

## JGR Solid Earth

## RESEARCH ARTICLE

10.1029/2018JB017035

## Key Points:

- Permeability of variably sintered tuffisites from Chaitén and Cordon Caulle is between  $10^{-16}$  and  $10^{-15}$  m<sup>2</sup>
- Surface tension and compaction-driven sintering timescales are between 2 min and 13.6 h and between 3.5 s and 5 min, respectively
- Inferred timescales of sintering-driven tuffisite compaction coincide with observed vent pulsations during hybrid rhyolitic activity

## Correspondence to:

M. J. Heap,  
heap@unistra.fr

## Citation:

Heap, M. J., Tuffen, H., Wadsworth, F. B., Reuschlé, T., Castro, J. M., & Schipper, C. I. (2019). The permeability evolution of tuffisites and implications for outgassing through dense rhyolitic magma. *Journal of Geophysical Research: Solid Earth*, 124, 8281–8299. <https://doi.org/10.1029/2018JB017035>

Received 13 NOV 2018

Accepted 26 JUL 2019

Accepted article online 31 JUL 2019

Published online 30 AUG 2019

# The Permeability Evolution of Tuffisites and Implications for Outgassing Through Dense Rhyolitic Magma

Michael J. Heap<sup>1</sup> , Hugh Tuffen<sup>2</sup>, Fabian B. Wadsworth<sup>3</sup> , Thierry Reuschlé<sup>1</sup>, Jonathan M. Castro<sup>4</sup>, and C. Ian Schipper<sup>5</sup>

<sup>1</sup>Institut de Physique de Globe de Strasbourg, Université de Strasbourg, École et Observatoire des Sciences de la Terre (UMR 7516 CNRS), Strasbourg, France, <sup>2</sup>Lancaster Environment Centre, Lancaster University, Lancaster, UK,

<sup>3</sup>Department of Earth Sciences, Durham University, Durham, UK, <sup>4</sup>Institute of Geosciences, Johannes Gutenberg University Mainz, Mainz, Germany, <sup>5</sup>School of Geography, Environment and Earth Sciences, Victoria University of Wellington, Wellington, New Zealand

**Abstract** There is growing evidence that outgassing through transient fracture networks exerts an important control on conduit processes and explosive-effusive activity during silicic eruptions. Indeed, the first modern observations of rhyolitic eruptions have revealed that degassed lava effusion may depend upon outgassing during simultaneous pyroclastic venting. The outgassing is thought to occur as gas and pyroclastic debris are discharged through shallow fracture networks within otherwise low-permeability, conduit-plugging lava domes. However, this discharge is only transient, as these fractures become clogged and eventually blocked by the accumulation and sintering of hot, melt-rich pyroclastic debris, drastically reducing their permeability and creating particle-filled tuffisites. In this study we present the first published permeability measurements for rhyolitic tuffisites, using samples from the recent rhyolitic eruptions at Chaitén (2008–2009) and Cordon Caulle (2011–2012) in Chile. To place constraints on tuffisite permeability evolution, we combine (1) laboratory measurements of the porosity and permeability of tuffisites that preserve different degrees of sintering, (2) theoretical estimates on grainsize- and temperature-dependent sintering timescales, and (3) H<sub>2</sub>O diffusion constraints on pressure-time paths. The inferred timescales of sintering-driven tuffisite compaction and permeability loss, spanning seconds (in the case of compaction-driven sintering) to hours (surface tension-driven sintering), coincide with timescales of diffusive degassing into tuffisites, observed vent pulsations during hybrid rhyolitic activity (extrusive behavior coincident with intermittent explosions), and more broadly, timescales of pressurization accompanying silicic lava dome extrusion. We discuss herein the complex feedbacks between fracture opening, closing, and sintering and their role in outgassing rhyolite lavas and mediating hybrid explosive-effusive activity.

## 1. Introduction

Unprecedented observations of recent subaerial rhyolite eruptions in Chile have demonstrated that effusive extrusion of rhyolitic lava can be coincident with intermittent explosions of ash, lapilli, and bombs (Castro et al., 2014; Lara, 2009; Schipper et al., 2013). Such hybrid activity demands reappraisal of existing paradigms of eruptive style transitions (Eichelberger et al., 1986) and highlights that outgassing mechanisms are of critical importance (e.g., Chevalier et al., 2017; Collinson & Neuberg, 2012; Farquharson et al., 2017; Gonnermann & Manga, 2003; Kushnir et al., 2017; Ryan et al., 2019). Chaitén volcano (Chile) exhibited prolonged hybrid activity in 2008 (Castro et al., 2014), whereas longer-lived hybrid (nine months) activity occurred at Cordon Caulle (also in Chile) during 2011–2012 (Schipper et al., 2013). In both cases pulsatory pyroclastic discharge occurred from fractures in vent-filling lava (Figure 1), a process now believed to have accompanied ancient silicic lava dome eruptions in other localities (e.g., Black et al., 2016). For example, the photograph taken during the 10 January 2012 activity at Cordon Caulle ( $t = +4$  s) shows that localized outgassing occurred via pathways with fracture (i.e., plane) geometries (Figure 1a), rather than outgassing through permeable foam (e.g., Eichelberger et al., 1986). Indeed, recent experimental work by Ryan et al. (2019) has shown that it is difficult to create permeability in initially impermeable, high-porosity foams, describing them as “persistently impermeable.” Dense obsidian bombs emitted during hybrid activity characteristically hosted tuffisites, which are centimetric fractures infilled with pyroclastic material (Castro et al., 2012; Heiken et al., 1988; Saubin et al., 2016; Stasiuk et al., 1996; Tuffen et al., 2003; Figure 2a). Tuffisites

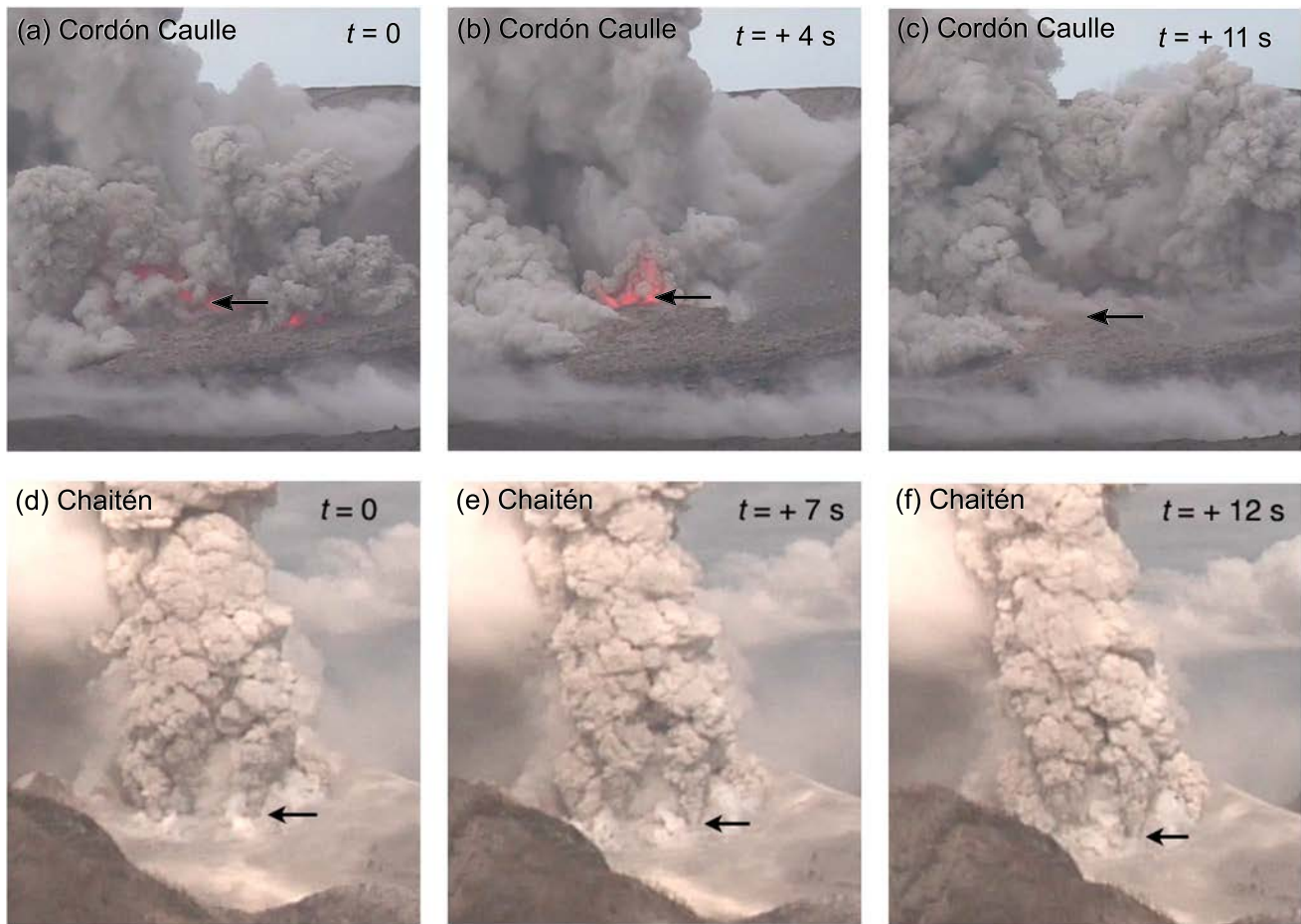


**Figure 1.** Explosive ash venting at (a) Cordón Caulle (10 January 2012) and (b) Chaitén (10 May 2008): (a)  $t = 0$  ash venting from a newly opened fracture (indicated by the arrow);  $t = 4$  ash venting reaches a climax; and  $t = 11$  ash venting from the fracture has stopped, highlighting the transient, pulsatory nature of the process. See also Schipper et al. (2013). (b) The time-stamped Chaitén frames illustrate the formation of a funnel shaped ash jet indicated by the arrow (scale 100 m). This jet is one of many pyroclastic vents that emanate from a lava plug that will days later form a voluminous obsidian dome.

have been interpreted to record the transient opening and occlusion of the permeable pathways that provide fleeting escape routes for pressurized gas prior to eventual blockage and violent ejection (Saubin et al., 2016).  $H_2O$  concentration gradients at the tuffisite-host rock interface (Berlo et al., 2013; Castro et al., 2012) and within fracture-filling clasts (Saubin et al., 2016) provide constraints on tuffisite depths (hundreds of meters), timescales of fracture opening (tens of minutes to several hours), and gas pressure changes associated with fracture opening (reductions of up to several MPa).

Modeling approaches (e.g., Collinson & Neuberg, 2012; Diller et al., 2006) and field measurements (e.g., Stix et al., 1993) have shown a low-permeability magmatic plug in the upper conduit can render outgassing ineffective, promoting gas accumulation and pressurization (a “closed system”). More recent modeling by Chevalier et al. (2017) has shown that although the dome can increase the pressure on the system and reduce gas loss at the conduit walls, the permeability of the conduit walls is of greater importance than the permeability of the dome in controlling gas loss and pressurization. In the case of a “closed system,” the initially highly permeable fracture networks, thought to be ultimately recorded as tuffisites, must play a key role in mediating gas release and pressurization cycles. Recent modeling by Farquharson et al. (2017), focused on the time-dependent permeability evolution of compacting fractured volcanic systems, defined three regimes: (1) an “outgassing” regime, where pore pressure does not increase during compaction; (2) a “diffusive relaxation” regime, where the ongoing reduction in porosity is compensated by the molecular diffusion of water; and



**Figure 2.** (a) Photograph of a large bomb in the crater of the 2008 Chaitén eruption containing a tuffisite (the parent of the BTB block). The BTB tuffisite is 30 mm wide with remarkably planar walls. It is connected to a network of sub-millimeter subsidiary tuffisites in the dense obsidian host material (Saubin et al., 2016). (b) Photograph of the decametric breadcrust bomb from the June 2011 hybrid activity at Cordón Caulle. (c) Photograph of a 20-mm-diameter cylindrical sample of tuffisite CH5F (Chaitén). (d) Photograph of a 20-mm-diameter cylindrical sample of tuffisite BTB (Chaitén). (e) Photograph of a 10-mm-diameter cylindrical sample of tuffisite CH5G (Chaitén). (f) Photograph of a 20-mm-diameter cylindrical sample of tuffisite B1 (Cordón Caulle).

(3) a “pore pressure increase” regime, where Darcian or diffusive processes cannot compensate for the porosity reduction and pore pressure builds. As improved modeling of conduit dynamics requires better constraints on the temporal evolution of tuffisite permeability, recent work has addressed the porosity and permeability of variably sintered pyroclastic material (Gardner et al., 2018; Heap et al., 2014, 2015; Kendrick et al., 2016; Kolzenburg & Russell, 2014; Okumura & Sasaki, 2014; Ryan, Friedlander, et al., 2018; Ryan, Russell, et al., 2018; Vasseur et al., 2013) and provided models of compaction and viscous sintering (i.e., the agglutination of glassy particles held at or above their corresponding glass transition temperature; Farquharson et al., 2017; Russell & Quane, 2005; Wadsworth et al., 2014; Wadsworth, Vasseur, Scheu, et al., 2016; Wadsworth, Vasseur, Llewellyn, et al., 2016; Wadsworth, Vasseur, Llewellyn, & Dingwell, 2017). These recent data and modeling provide a blueprint for placing firmer constraints on permeability evolution within volcanic conduits.

We present herein porosity and permeability measurements for tuffisites hosted within dense obsidian bombs ejected from recent rhyolitic eruptions at Chaitén (2008–2009) and Cordón Caulle (2011–2012). These data, which represent the first permeability measurements of rhyolite-hosted tuffisites, are combined with models for viscous sintering and pressure timescale constraints from  $H_2O$  diffusion gradients to provide a detailed description of tuffisite permeability evolution and thus explore the role of fracture-assisted outgassing within shallow silicic conduits.

## 2. Anatomy of a Tuffisite

Three rhyolitic tuffisites (CH5F, BTB, and CH5G) hosted within decametric dense obsidian bombs that were ejected during hybrid activity in May 2008 at Chaitén volcano (an example is provided as Figure 2a) and found within the pyroclastic density current deposits about 800 m from the 2008–2009 vent were selected for this study. Several field campaigns at Chaitén volcano have highlighted that bombs on the crater rim and flanks commonly host tuffisites. The width of these tuffisites typically ranged from a couple of millimeters up to a few tens of millimeters. The tuffisites within these bombs comprise poorly sorted and variably sintered angular fragments of dense obsidian, pumice, and lithics within a fine ash grade matrix (Figure 2a). The three samples chosen for this study were selected because of visible differences in density/porosity (photographs of core samples prepared from these three tuffisites are provided as Figures 2c–2e), suggesting underlying differences in their degree of sintering. As a result, we consider that these samples provide snapshots in time of the viscous sintering process. We complement these samples with a tuffisitic bomb fragment from Cordón Caulle, part of a decametric breadcrust bomb found 1.5 km NW of the vent (Figure 2b). The bomb was ejected between 7 and 15 June 2011, as the vent constricted prior to and during the onset of lava effusion and thus hybrid activity. It comprises glassy, tuffisitic material that has partly vesiculated after fragmentation, with inflation of the largest, most volatile-rich clasts (Figures 2b and 2f).



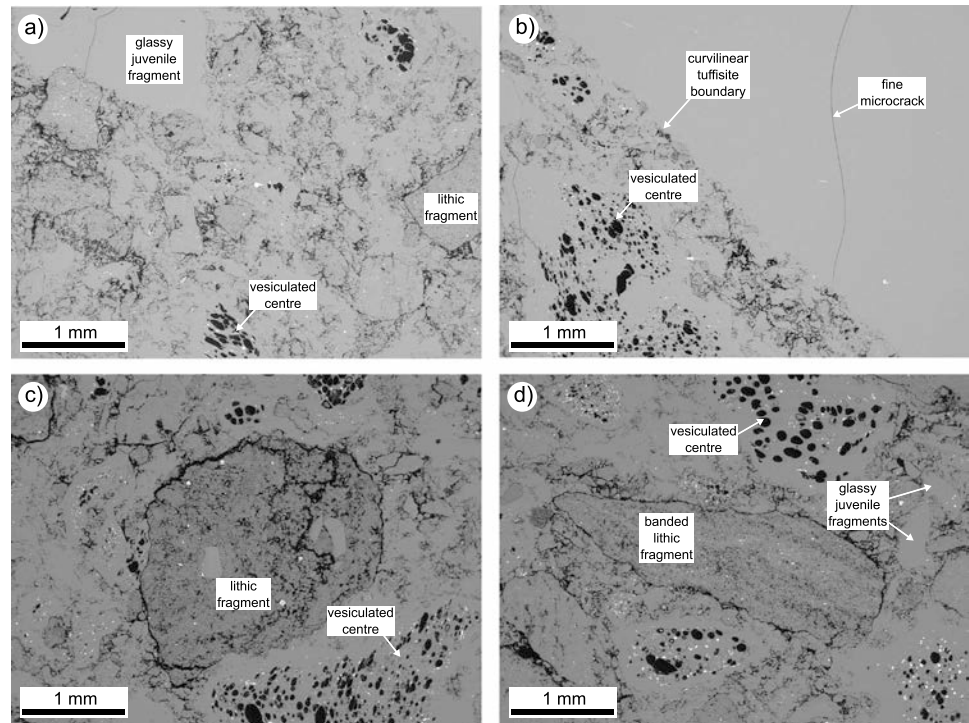


**Figure 3.** Backscattered scanning electron microscope images of the BTB tuffisite. The images show that the BTB tuffisite contains mixture of ash- and lapilli-sized juvenile and lithic fragments. Some of the juvenile fragments have vesiculated centers (a–d). Lithic clasts (rhyolite fragments) can be rounded (c) or banded/angular (d). Panel (b) shows that the tuffisite-host rock boundary is curvilinear on the microscale.

Backscattered scanning electron microscope images of the four tuffisites were collected using a Tescan Vega 2 XMU system, and representative tuffisite textures are shown in Figures 3 and 4. The tuffisites comprise a similar population of ash- and lapilli-sized juvenile and lithic fragments (Figures 3 and 4). The juvenile fragments within the tuffisites are glassy and often angular, but their edges can be rounded or diffuse, depending on the degree of viscous sintering. For example, the sintering of juvenile clasts in sample CH5F is sufficiently advanced that it is difficult to distinguish individual fragments (Figures 4a and 4b), with remaining porosity preferentially located at the margins of lithic clasts (Figure 4b). Viscous sintering is least well developed in sample CH5G, with individual glassy juvenile fragments often easily identifiable (Figure 4c and 4d). Indeed, the matrix porosity is noticeably higher in the CH5G sample than the other three samples and is not restricted to lithic clast margins (Figure 4c and 4d). Individual glassy particles in sample B1 appear rounded and are only distinguishable because of the interstitial pore space, which has been compacted and deformed (Figure 4f).

Some juvenile clasts in the BTB (Figure 3), CH5G (Figure 4d), and B1 (Figures 4e and 4f) samples have vesiculated centers leading to a frothed appearance. Quantification of vesicle size distributions and  $H_2O$  concentrations in sample BTB (Saubin et al., 2016) has facilitated a detailed reconstruction of the relative timing of clast vesiculation and fracture opening, together with the evolution of gas pressure in the system. Results show that, for sample BTB, the strongly vesiculated clasts had vesiculated prior to their incorporation into the fracture by pressurized gas from deeper in the conduit. However, it is likely that the common vesiculated juvenile clasts in sample B1 (Figure 4e) have predominantly vesiculated after bomb ejection. Vesiculated juvenile clasts are rare in sample CH5F (Figures 4a and 4b).

Lithic fragments in these tuffisites can be angular, but they are often subrounded (Figures 3 and 4). Most lithics are rhyolite fragments that are banded and microporous with cristobalite and minor plagioclase phases protruding into pore spaces (Figures 3 and 4). Finally, we highlight that the boundary

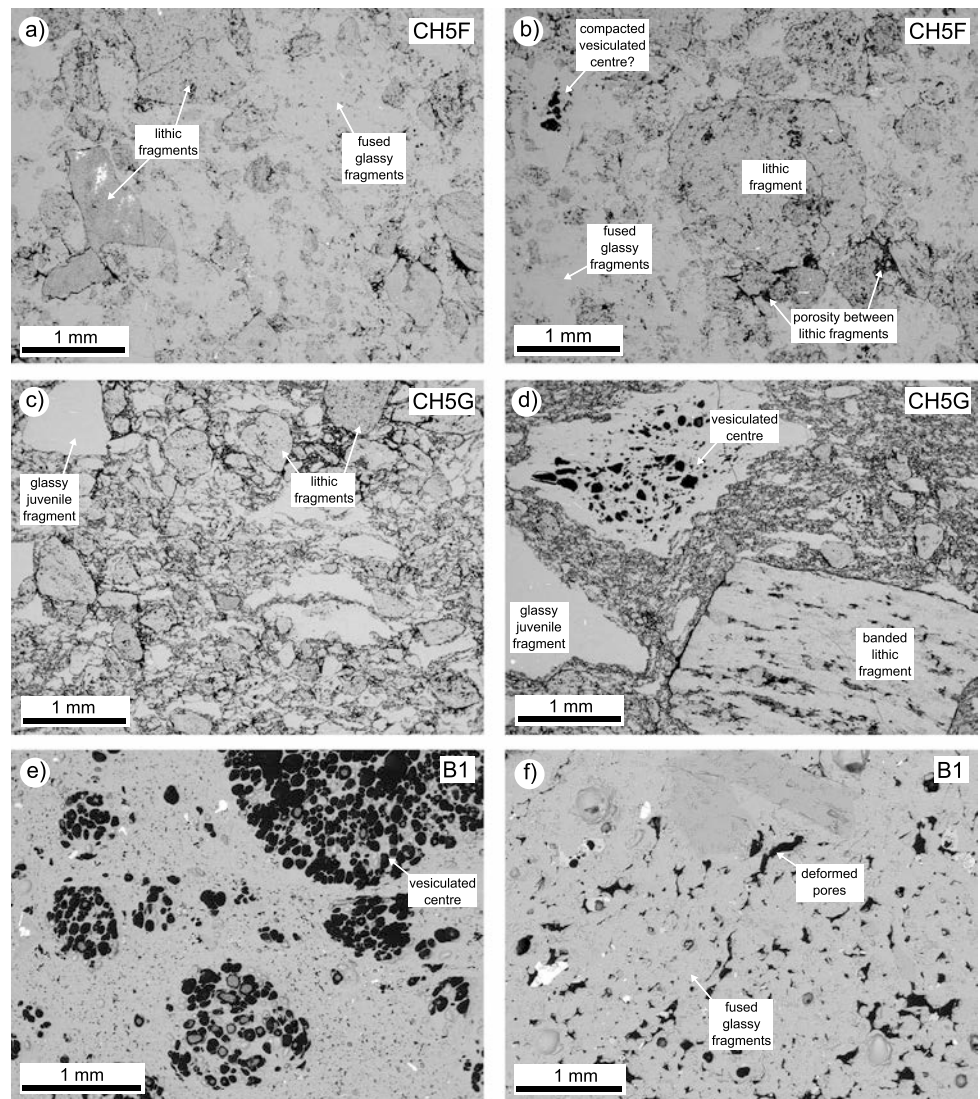


**Figure 4.** Backscattered scanning electron microscope images of the CH5F (a, b), the CH5G (c, d), and the B1 (e, f) tuffisites. The images show that the tuffisites contain mixture of ash- and lapilli-sized juvenile and lithic fragments. Lithic clasts (rhyolite fragments) can be rounded (b and c) or banded/angular (a and d). Juvenile fragments with vesiculated centers can be seen in samples CH5G (d) and B1 (e), but are rare in sample CH5F (b). Glassy fragments are angular in sample CH5G (c, d), have diffuse boundaries in sample CH5F (a, b), and appear rounded in sample B1 (f).

between the tuffisite and the obsidian host rock is curvilinear on the microscale (Figure 3b). Further details on the clast population within the BTB tuffisite, including grainsize distribution and componentry, and the relationship between the timing of fracture opening and clast vesiculation, can be found in Saubin et al. (2016).

### 3. Experimental Methods

Cylindrical samples (either 20 or 10-mm diameter) of the tuffisitic material were cored from each bomb. Samples were cored such that their axis is parallel to the fracture plane, so as to maximize the number of samples extracted from each of the blocks collected (see inset on Figure 2a). Samples from the Cordón Caille bomb were prepared to avoid large vesiculated fragments and the approximately decameter-spaced cooling contraction fractures associated with breadcrusting (see Figure 2b). We also prepared a 20-mm-diameter sample of the dense obsidian host rock from the BTB bomb. These samples were precision

ground to lengths of 30–40 mm (for the 20-mm-diameter samples) or 20–40 mm (for the 10-mm-diameter samples) and dried for a minimum of 48 hr inside a vacuum oven at 40 °C. All samples were prepared such that their length-diameter ratio is greater than one. Recent experiments by Heap (2019) highlighted that reliable laboratory measurements of permeability are possible on small cores (e.g., 10-mm-diameter cores) as long as the pore/grain size is small with respect to the core dimensions.

The connected porosity and permeability was then measured for each cylindrical sample. The connected porosity of each sample was calculated using the bulk volume of the sample (calculated using the sample dimensions) and the skeletal (i.e., connected) volume given by a Micromeritics AccuPyc II 1340 helium pycnometer. The total porosity of each sample was determined using the solid density of each block (measured using a hand-powdered aliquot of each sample and the helium pycnometer) and the bulk sample density of each cylindrical sample (calculated using the mass and dimensions of each sample). The isolated porosity of each sample could then be determined by subtracting the connected porosity from the total porosity. Permeability was measured using a gas (argon or nitrogen) permeameter following the operating procedure given in Farquharson et al. (2016) and Heap and Kennedy (2016). Permeability was measured under a confining pressure of 1 MPa (a confining pressure is needed to ensure that the gas travels through the sample, rather than between the jacket and the sample edge) using the steady state method. The permeability of a sample of BTB was also measured under confining pressures up to 10 MPa to cover the range of pressures inferred during tuffsite formation (equivalent to 400- to 500-m lithostatic; Castro et al., 2014; Saubin et al., 2016) and using the same procedure described above.

To measure permeability, the volumetric flow rate,  $Q_v$  (in  $\text{m}^3/\text{s}$ ) was measured using a gas flowmeter for several different pressure differentials,  $\Delta P$  (we define  $\Delta P$  as the upstream pore fluid pressure,  $P_u$  [in Pa], minus the downstream pore fluid pressure,  $P_d$  [in Pa]). In our permeameter setup,  $P_d$  is the atmospheric pressure (assumed to be 101,325 Pa). The Darcian permeability,  $k_D$  (in  $\text{m}^2$ ), was then determined for each of the pressure differentials using the following relationship for compressible gas:

$$k_D = \frac{Q_v}{P_m \Delta P} \frac{\mu L P_d}{A}, \quad (1)$$

where  $\mu$  is the pore fluid viscosity (viscosity of argon and nitrogen at 20 °C was taken as  $2.22 \times 10^{-5}$  and  $1.76 \times 10^{-5}$  Pa s, respectively; values taken from the National Institute of Standards and Technology, <https://www.nist.gov/>),  $A$  (in  $\text{m}^2$ ) and  $L$  (in m) are the sample cross sectional area and the sample length, respectively, and  $P_m$  is the mean pore fluid pressure (i.e.,  $(P_u + P_d)/2$ ). We calculate  $k_D$  for a range of different pressure differentials (typically six) to assess whether fluid flow departs from Darcian flow (i.e., equation (1)). We assume a constant pore fluid density and viscosity for our measurements, a valid assumption for the very low pressure differentials used in this study (the pressure differential never exceeded 0.5 MPa). Fluid flow can be complicated by gas slippage (the Klinkenberg effect; Klinkenberg, 1941) and/or by turbulence (the Forchheimer effect; Forchheimer, 1901). We first check whether a Forchheimer correction is needed. To do so, we plot  $1/k_D$  for each pressure differential,  $\Delta P$ , as a function of  $Q_v$ . If these data can be well described by a positive linear slope, the Forchheimer-corrected permeability  $k_{\text{forch}}$  is the inverse of the y intercept of the best fit linear regression of this relationship. If the Forchheimer correction is needed, it is then necessary to check whether the Klinkenberg correction is needed. To check whether the Klinkenberg correction is needed, we calculate  $k_{\text{forch}}$  for each pressure differential,  $\Delta P$ , using the following relation:

$$\frac{1}{k_D} = \xi Q_v + \frac{1}{k_{\text{forch}}}, \quad (2)$$

where the slope of the plot of  $1/k_D$  as a function of  $Q_v$  is given by  $\xi$ . The Klinkenberg correction is needed if the data on a plot of  $k_{\text{forch}}$  as a function of  $1/P_m$  can be well described by a positive linear slope. If this is true, the permeability is the y intercept of the best fit linear regression of these data. If the data cannot be well described by a positive linear relationship, the permeability is the inverse of the y intercept of the best fit linear regression on the plot of  $1/k_D$  as a function of  $Q_v$  (i.e.,  $k_{\text{forch}}$ ). If the Forchheimer correction is not needed, we assess the need for the Klinkenberg correction by plotting  $k_D$  as a function of  $1/P_m$ . If the data can well described by a positive linear slope, a Klinkenberg correction is required and the permeability is the y intercept of the best fit linear regression on the graph of  $k_D$  as a function of  $1/P_m$ . If no corrections are needed, the permeability is



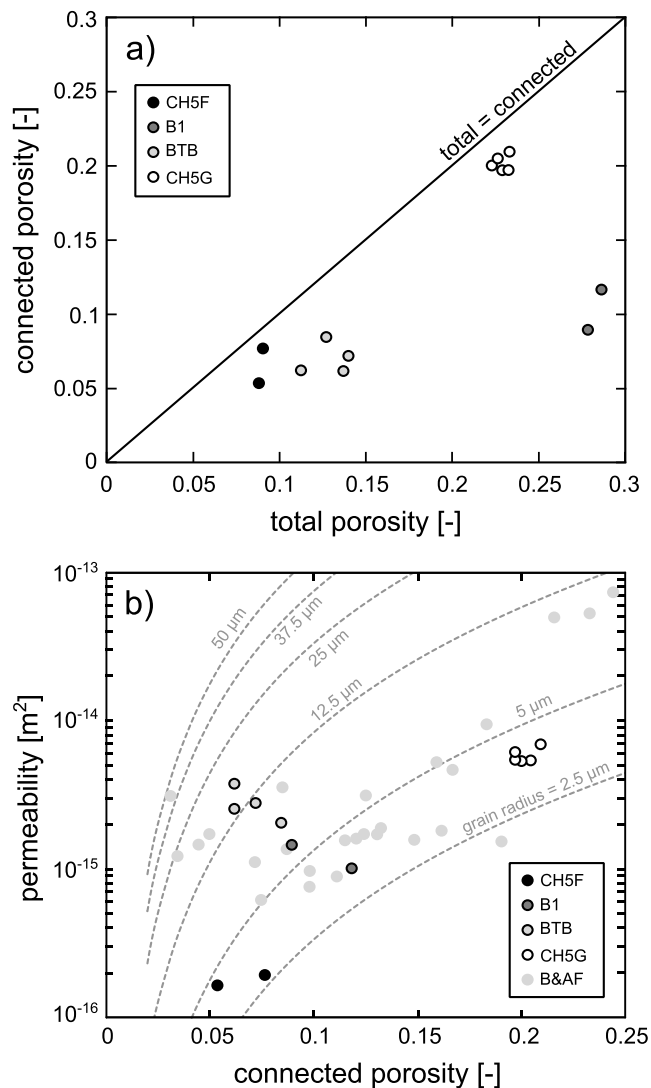


**Figure 5.** (a) Connected porosity as a function of total porosity for the four tuffisite samples (BTB, CH5F, CH5G, and B1). Measurement errors are smaller than the symbol size. (b) Permeability as a function of porosity for the four tuffisite samples (BTB, CH5F, CH5G, and B1). Measurement errors are smaller than the symbol size. Model curves (equation (5)) for a given initial particle radii are also provided as grey dashed lines (Wadsworth, Vasseur, Scheu, et al., 2016; see discussion for details). Data for variably sintered, granular volcanic material (welded block-and-ash flow; B&AF) from Heap et al. (2015) are plotted to provide a comparison (light grey circles).

taken as the positive slope of the plot of  $Q_v$  as a function the mean pore fluid pressure  $P_m$  multiplied by  $\Delta P$ . These ancillary corrections were implemented on a case-by-case basis (we refer the reader to Heap, Reuschlé, Farquharson, et al., 2018, for examples). The values of the coefficient of determination ( $R^2$ ) for the best fit regressions, when applied, were between 0.98 and 0.99, where a value of unity represents perfect agreement. A more detailed description of our permeability data analysis technique can be found in Heap et al. (2017).

To assess the size of the smallest pore apertures of a tuffisite, we performed mercury injection porosimetry on a piece (4.7 g) of the BTB sample using a Micromeritics Autopore IV 9500. The mercury equilibration time and filling pressure were 10 s and  $\sim 3,585$  Pa, respectively. The evacuation time and evacuation pressure were 5 min and  $50 \mu\text{mHg}$ , respectively. The pressure range was  $\sim 690$  Pa up to  $\sim 414$  MPa. Data from a mercury injection test were used to calculate the pore throat size distribution of the sample (ASTM D4404-10, 2010). We corrected the mercury injection data for the “low pressure correction,” as recommended by the American Society for Testing and Materials (ASTM D4404-10, 2010).

The dissolved  $\text{H}_2\text{O}$  concentration was measured along a profile from the boundary of the tuffisite in the CH5G sample (position of the profile is shown on an inset in Figure 6c) using synchrotron source Fourier transform infrared spectroscopy at the Diamond Light Source (UK) MIRIAM beamline. A Hyperion 3000 microscope with a broadband MCT detector was coupled to a Bruker Vertex 80 V Fourier transform infrared spectroscopy interferometer with KBr beamsplitter. A  $10\text{-}\mu\text{m}$  square aperture was used and 128 spectra were collected in transmission mode at  $8 \text{ cm}^{-1}$  spectral resolution between  $4,000$  and  $1,000 \text{ cm}^{-1}$ . Wafer thickness (average thickness of  $90 \mu\text{m}$ ) was measured using either a digital micrometer (precision  $\pm 3 \mu\text{m}$ ) or by the reflection fringe method (von Aulock et al., 2014). Peak heights at  $3,550 \text{ cm}^{-1}$  ( $\text{H}_2\text{O}_l$ ) and  $1,630 \text{ cm}^{-1}$  ( $\text{H}_2\text{O}_m$ ) were determined using 18-point linear baseline corrections. Using the Beer-Lambert law, a glass density of  $2,281 \text{ kg/m}^3$  (Saubin et al., 2016), and absorption coefficients of  $80 \text{ l mol}^{-1}/\text{cm}$  ( $3,550 \text{ cm}^{-1}$ ; Ihinger et al., 1994) and  $55 \text{ l mol}^{-1} \text{ cm}$  ( $1,630 \text{ cm}^{-1}$ ; Newman et al., 1986; Okumura et al., 2003), we converted these data to species concentrations. The combined uncertainty of this method, which depends on the wafer thickness and density and the choice of molar absorption coefficient, is typically  $<10\%$  (von Aulock et al., 2014). We compare these data with those already collected for the BTB sample (presented in Saubin et al., 2016) using the same technique.

## 4. Results

Connected porosity as a function of total porosity is shown in Figure 5a (data available in Table 1). The connected porosity of these tuffisites varies from  $\sim 0.05$  to  $\sim 0.2$  (Figure 5a and Table 1). All of the measured tuffisites contain isolated porosity. The three samples from Chaitén contain isolated porosities between  $\sim 0.01$  and  $\sim 0.075$ , whereas the B1 sample from Cordón Caulle contains a very high isolated porosity of  $\sim 0.17\text{--}0.19$  (Figure 5a and Table 1).

Permeability as a function of connected porosity is shown in Figure 5b (data available in Table 1). CH5G contains the largest connected porosity ( $\sim 0.2$ ) and has the largest permeability ( $\sim 6 \times 10^{-15} \text{ m}^2$ ). Although BTB and CH5F contain similar connected porosities ( $\sim 0.07$ ), BTB is approximately an order of magnitude more permeable ( $\sim 3 \times 10^{-15} \text{ m}^2$  compared to  $\sim 6 \times 10^{-16} \text{ m}^2$ ; Figure 5b and Table 1). The connected porosity of B1 is larger (up to  $\sim 0.12$ ) than both CH5G and BTB but has a permeability close to that of BTB (Figure 5b and

**Table 1**  
Summary of the Porosity/Permeability Measurements Performed for This Study

Sample	Total porosity	Connected porosity	Isolated porosity	Confining pressure (MPa)	Pore fluid	Permeability (m <sup>2</sup> )	Correction	Klinkenberg factor (MPa)	slip	Average radius (μm)	pore
BTB-01	0.127	0.085	0.042	1	Argon	$2.04 \times 10^{-15}$	Klinkenberg	0.0365		0.75	
BTB-01	0.127	0.085	0.042	2	Argon	$1.93 \times 10^{-15}$	Klinkenberg	0.0375		0.73	
BTB-01	0.127	0.085	0.042	4	Argon	$1.84 \times 10^{-15}$	Klinkenberg	0.0385		0.71	
BTB-01	0.127	0.085	0.042	6	Argon	$1.80 \times 10^{-15}$	Klinkenberg	0.0385		0.71	
BTB-01	0.127	0.085	0.042	8	Argon	$1.77 \times 10^{-15}$	Klinkenberg	0.0390		0.70	
BTB-01	0.127	0.085	0.042	10	Argon	$1.73 \times 10^{-15}$	Klinkenberg	0.0390		0.70	
BTB-02	0.140	0.072	0.068	1	Nitrogen	$2.77 \times 10^{-15}$	Forchheimer	—		—	
BTB-03	0.113	0.062	0.051	1	Nitrogen	$2.54 \times 10^{-15}$	Forchheimer	—		—	
BTB-04	0.137	0.062	0.075	1	Nitrogen	$3.73 \times 10^{-15}$	Forchheimer	—		—	
BTB-07	0	0	0	1	Nitrogen	0	—	—		—	
CH5_F-01	0.090	0.077	0.014	1	Nitrogen	$1.91 \times 10^{-16}$	None	—		—	
CH5_F-02	0.088	0.054	0.034	1	Nitrogen	$1.63 \times 10^{-16}$	None	—		—	
CH5_G-01	0.232	0.197	0.035	1	Nitrogen	$6.12 \times 10^{-15}$	Forchheimer	—		—	
CH5_G-02	0.223	0.200	0.023	1	Nitrogen	$5.33 \times 10^{-15}$	Forchheimer	—		—	
CH5_G-03	0.226	0.205	0.022	1	Nitrogen	$5.37 \times 10^{-15}$	Forchheimer	—		—	
CH5_G-04	0.233	0.209	0.023	1	Nitrogen	$6.87 \times 10^{-15}$	Forchheimer	—		—	
CH5_G-05	0.229	0.197	0.031	1	Nitrogen	$5.40 \times 10^{-15}$	Forchheimer	—		—	
B1	0.286	0.118	0.170	1	Nitrogen	$1.03 \times 10^{-15}$	Forchheimer	—		—	
B1	0.278	0.090	0.189	1	Nitrogen	$1.48 \times 10^{-15}$	Forchheimer	—		—	

Note. Porosities quoted were measured at ambient laboratory pressure; the quoted confining pressure refers to the pressure used for the permeability measurements. Average pore radii were estimated using the Klinkenberg slip factor (see equation (4) and text for details).

Table 1). The porosity and permeability of the obsidian host were found to be within error of zero (Table 1). Data at elevated confining pressure show that tuffisite permeability does not change significantly up to 10 MPa (Figure 6a). The permeability of the BTB sample was reduced from  $2.04 \times 10^{-15}$  m<sup>2</sup> at a confining pressure of 1 MPa to  $1.73 \times 10^{-15}$  m<sup>2</sup> at a confining pressure of 10 MPa (Figure 6a and Table 1).

The data from the mercury injection experiment (Figure 6b) indicate that about 8% of the connected void volume is connected by pore throats that are >5 μm in radius, 72% of the connected void volume is connected by pore throats between 0.05 and 5 μm in radius, and 20% of the connected void volume is connected by pore throats <0.05 μm in radius.

In sample CH5F, the H<sub>2</sub>O concentration is 0.46 wt.% at the tuffisite boundary and reaches a constant value of 1.04 wt.% at ~400 μm from the boundary (black symbols on Figure 6c). The H<sub>2</sub>O concentration in the BTB sample (data from Saubin et al., 2016) is ~0.65 wt.% at the boundary of a vesicular clast and increases to ~0.9 wt.% at a distance of ~100 μm (grey symbols on Figure 6c).

## 5. Discussion

### 5.1. Isolated Porosity Within the Tuffisites

Our data show that all of the measured tuffisites contain isolated porosity (Figure 5a and Table 1). The high isolated porosity of these samples is due to the presence of vesiculated juvenile clasts, which typically contain glassy rim with a porosity and therefore permeability of zero (Figures 3 and 4). Sample B1, from Cordón Caille, contains abundant vesiculated juvenile clasts (Figures 4e and 4f) and, as a result, contains the largest isolated porosity of ~0.17–0.19 (Figure 5a and Table 1). Since the porosity in these clasts is isolated (encapsulated within a zero porosity glassy rim; Figures 3 and 4), it does not therefore contribute to the permeability of the samples.



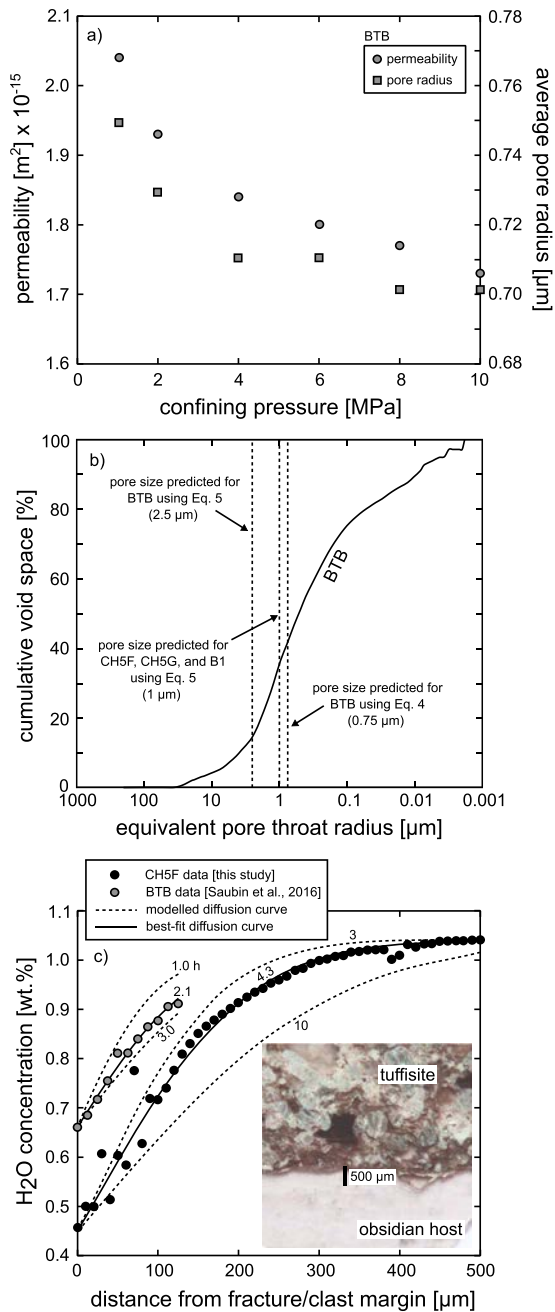


**Figure 6.** (a) Permeability as a function of confining pressure (up to 10 MPa) for a sample of BTB. Also shown is the average pore radius used by the gas molecules, as calculated using the Klinkenberg slip factor (equation (4); see discussion for details). (b) Pore throat size distribution (plot of cumulative void space as a function of pore throat diameter) determined using mercury porosimetry. The pore throat diameters determined using the Klinkenberg analysis (equation (4)) and the permeability modeling (equation (5)) are also indicated on the plot. (c) Measured spatial variation in H<sub>2</sub>O from a clast margin for BTB (data from Saubin et al., 2016) and from the host rock obsidian for CH5F. Best-fit modeled 1-D diffusion curves (solid lines) are given for each dataset (number in hours; see discussion for details). We also provide neighboring modeled 1-D diffusion curves (dashed lines; number in hours; see discussion for details). Inset on panel (c) shows a photograph showing the location of the profile in sample CH5F. Images of the transect for the BTB sample can be found in Saubin et al. (2016).

## 5.2. Permeability Modeling: Pore and Grainsize Analyses

The collected porosity and permeability data can be interrogated to better understand (1) the average pore radius used by the gas molecules to travel through the tuffisite and (2) the particle size that likely controls the efficiency of viscous sintering.

First, we estimate of the average radius of the pores used by the gas molecules using the Klinkenberg slip factor,  $b$  (a calculation only possible for the data that required a Klinkenberg correction, see Table 1). Since the mean free path is inversely proportional to the mean pore fluid pressure, Poiseuille's law for gas flow in a cylindrical tube and Darcy's law for flow in a porous medium provide the following relation:

$$k_{\text{klink}} = k_D \left( 1 + \frac{b}{P_m} \right), \quad (3)$$

where  $k_{\text{klink}}$  is gas permeability corrected by the Klinkenberg correction (see section 3 for details). Assuming a cylindrical pore shape, the average pore radius  $a$  used by the gas molecules can then be estimated using the following relationship (Civan, 2010; Firouzi et al., 2014):

$$a = \frac{4}{b} \mu \sqrt{\frac{\pi R_g T}{2 M_w}}, \quad (4)$$

where  $T$  is the temperature (293 K for room temperature laboratory conditions),  $M_w$  is the molar mass of the argon pore fluid (0.03995 kg/mol), and  $R_g$  is the ideal gas constant (8.31 J mol<sup>-1</sup> K<sup>-1</sup>). This method has been used to estimate the average pore radius of the flow path in shales (e.g., Firouzi et al., 2014; Heller et al., 2014; Letham & Bustin, 2016), volcanic rocks (Heap, Reuschlé, Farquharson, et al., 2018), and limestones (Heap, Reuschlé, Baud, & et al., 2018). We find an average pore radius of 0.75 μm for the BTB sample at a confining pressure of 1 MPa (Figure 6a). The average pore radius estimated using equation (4) is reduced only slightly (to 0.70 μm) when the confining pressure is increased to 10 MPa (Figure 6a). The average pore radius estimated using the Klinkenberg slip factor highlights the complexity of the flow path within the BTB tuffisite. For example, although 40% of the void space within the tuffisite is connected by pore throats with a radius greater than 1 μm (Figure 6b), the gas travels through narrow microstructural elements (with a radius <1 μm). Because the permeability and the average pore radius used by the gas do not vary considerably with pressure (Figure 6a), it is likely that these narrow microstructural elements are the tortuous intergranular pores characteristic of sintering systems (microcracks are easily closed as confining pressure is increased; e.g., Nara et al., 2011). These data therefore highlight that our measurements at 1 MPa are relevant for in situ tuffisites and that their compressibility is low even under relevant upper conduit pressures.

Wadsworth, Vasseur, Scheu, et al. (2016) provide a model for predicting first the characteristic lengthscale of the pore network,  $1/s$ , and second the permeability,  $k_D$ , of sintered granular materials for which the inter-grain spaces are the pore network. The modeled permeability is given by (Wadsworth, Vasseur, Scheu, et al., 2016)

$$k_D = \frac{2[1 - (\phi - \phi_c)]}{s^2} (\phi - \phi_c)^e, \quad (5)$$

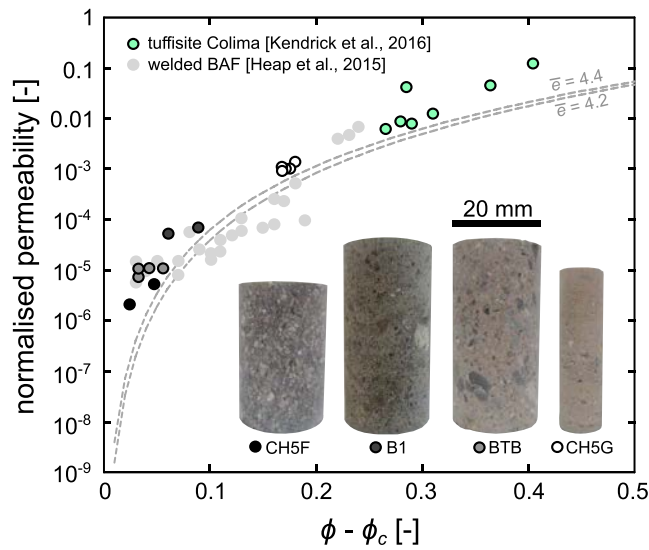


**Figure 7.** Normalized permeability (see text for details) as a function of  $\phi - \phi_c$  (porosity minus the porosity of the percolation threshold at which the permeability can be considered zero, taken here as  $\phi_c = 0.03$ ). The circles represent the experimental data (data unique to this study and data from Heap et al., 2015, and Kendrick et al., 2016) and collapse to a single permeability description consistent with  $4.2 < \bar{e} < 4.4$  (the two grey dashed curves; see text for details).

where  $s$  is the specific surface area, that is, the ratio of pore surface area within the sample to the sample volume (in  $\text{m}^{-1}$ ),  $\phi_c$  is the porosity of the percolation threshold at which the permeability can be considered zero, and  $\bar{e}$  is a percolation exponent. As noted by Wadsworth, Vasseur, Scheu, et al. (2016), this model has the appealing features that the permeability falls to zero as  $\phi \rightarrow \phi_c$ , and for all  $\phi$  above  $\phi_c$ , it has a power law dependence on  $\phi$ , for which the exponent is  $\bar{e}$ , similar to theoretical constraints (Feng et al., 1987). Feng et al. (1987) constrained  $\bar{e} = 4.4$  based on theoretical scaling, while empirical fits to a large range of data collected for variably welded granular rocks yield  $\bar{e} = 4.2 \pm 0.3$  (Wadsworth, Vasseur, Scheu, et al., 2016).  $\phi_c$  is typically around 0.03 for initially granular systems (Rintoul, 2000; Wadsworth, Vasseur, Llewellyn, et al., 2016). The specific surface area is then related to the pore radius via  $s = 3(1 - \phi) \ln(1 - \phi)/a$  assuming that the pore network can be approximated as a pack of overlapping spherical pores (see Torquato, 2013). Finally, the pore radius  $a$  is predicted at the initial packing porosity ( $\phi_i = 0.5$ ) from the grainsize distribution, using the mean of the distribution  $R$  and the porosity after Torquato and Avellaneda (1991), with the full solution provided in Wadsworth, Vasseur, Scheu, et al. (2016). We then compare the modeled permeability curves (using equation (5)), solved for a range of mean grain-size  $R$ , with our porosity and permeability measurements for the tuffisite samples (Figure 5b). The measured porosity and permeability data are consistent with initial grain radii of  $2.5 < R < 15 \mu\text{m}$

(Figure 5). Although these inferred radii are small compared to the fragments readily identifiable in our microstructural work (Figures 3 and 4), they are consistent with previous measurements of the fine fraction that dominates the matrix in the BTB sample (Saubin et al., 2016). This range of predicted grainsizes is therefore likely to represent the grainsize that controls the efficiency of viscous sintering—a result of the inverse grainsize dependence of the sintering rate (Wadsworth et al., 2014). The grainsizes predicted using this approach are similar to those predicted for similar variably sintered, granular volcanic material (welded block-and-ash flow deposits, BAF, from Mt. Meager in Canada; data taken from Heap et al., 2015), shown as light grey circles in Figure 5b.

Next we use an empirical fitting procedure to predict the pore radii for each tuffisite. We assume that equation (5) is a valid description of the permeability as a function of the porosity and that  $\bar{e} = 4.2$  and  $\phi_c = 0.03$ . We use the Excel Solver tool to minimize for a single controlling value of  $s$  for each sample and to assess the uncertainties that result using the method outlined in Kemmer and Keller (2010). This yields a fitted  $s$  that can be converted to a mean pore radius characteristic of flow through the sample using the above  $s(a, \phi)$  result. The output is  $a = 2.5 \pm 0.9 \mu\text{m}$  for the BTB sample and  $a = 1.0 \pm 0.4 \mu\text{m}$  for the CH5F, CH5G, and B1 samples. This provides a natural method to normalize the permeability by  $ks^2/(2[1 - (\phi - \phi_c)])$ . In Figure 7 we demonstrate that this method results in a collapse of the data to a single permeability description that is consistent with both  $4.2 < \bar{e} < 4.4$ , as predicted by theory (Feng et al., 1987; Wadsworth, Vasseur, Llewellyn, & Dingwell, 2017; Wadsworth, Vasseur, Scheu, et al., 2016). We also plot the welded block-and-ash flow data from Heap et al. (2015) and the data for tuffisites found on the dome of Volcán de Colima, an andesitic stratovolcano in Mexico (permeability measured using the TinyPerm II field permeameter; Kendrick et al., 2016). These data also collapse on our permeability description (Figure 7). Additionally, the pore radii resulting from this method ( $1\text{--}2.5 \mu\text{m}$ ) are within a factor of 2 of those calculated from the Klinkenberg factor ( $0.7\text{--}0.75 \mu\text{m}$ ) and within the range measured by mercury injection porosimetry (Figure 6b).

The above approach provides several methods for predicting the controlling lengthscales for fluid flow through samples of this type, including direct measurements. We have shown that use of equation (5) results in good collapse of the data (and data for other welded volcanic materials and tuffisites from Mt. Meager and Volcán de Colima, respectively; Figure 7) to a single dimensionless description, which lends confidence to the

generality of this model. We propose that this may be a useful tool for predicting the permeability decay of evolving tuffisites as they sinter and heal in silicic volcanoes.

### 5.3. H<sub>2</sub>O Diffusion Modeling

Modeling the depletion in H<sub>2</sub>O adjacent from the tuffisite-host rock boundary, or from the boundary of a vesicular clast within the tuffisite, provides an estimate of the time between fracture filling and final quenching (e.g., Castro et al., 2012). Our modeling of the H<sub>2</sub>O diffusion profiles employed an error function solution to Fick's general diffusion equation cast in 1-D Cartesian coordinates for a constant diffusivity (after Crank, 1979):

$$\frac{c_x - c_b}{c_0 - c_b} = 1 - \operatorname{erf} \left[ \frac{x}{2\sqrt{Dt}} \right], \quad (6)$$

where  $c_x$  denotes the concentration of H<sub>2</sub>O (in wt.%) at a distance of  $x$  from the fracture/clast boundary (m),  $c_b$  is the H<sub>2</sub>O concentration of the far field in the host obsidian (in wt.%),  $c_0$  is the (lower) H<sub>2</sub>O concentration within the tuffisite defining the limit at the tuffisite wall (in wt.%),  $t$  is time (s), and the H<sub>2</sub>O diffusivity ( $\text{m}^2/\text{s}$ ) is given by  $D$ . H<sub>2</sub>O molecules were assumed to be the only species diffusing (e.g., Behrens & Nowak, 1997) and the magmatic temperature was assumed to be constant at 825 °C (a value constrained by the petrological experiments of Castro & Dingwell, 2009). Boundary conditions were fixed at the far-field H<sub>2</sub>O concentration  $c_0$ , as defined from diffusion profiles, and the lowest H<sub>2</sub>O concentration  $c_b$  as measured at the fracture/clast boundary. The H<sub>2</sub>O diffusivity was calculated using the concentration- and temperature-dependent model for rhyolitic melt of Zhang (1999):

$$D_{\text{H}_2\text{O}_t} = \left( \frac{c}{c_r} \right) \exp \left[ -16.83 - \frac{10992}{T} \right], \quad (7)$$

where  $c$  is the local H<sub>2</sub>O concentration (in wt.%),  $c_r$  is a reference H<sub>2</sub>O concentration of 1 wt.% (see Figure 6c and Zhang, 1999), and  $T$  is the temperature (K). As the error function diffusion solution assumes a constant diffusivity, which we take to be the diffusivity calculated using equation (7) for a value of  $c = 0.75$  wt.%, which is the arithmetic mean of the measured  $c_0$  and  $c_b$  (yielding  $D_{\text{H}_2\text{O}_t} = 1.6 \times 10^{-12} \text{ m}^2/\text{s}$ ). Because the difference between diffusivities at  $c_0$  and  $c_b$  is modest ( $1 \times 10^{-12} \text{ m}^2/\text{s}$  at 0.46 wt.% H<sub>2</sub>O, and  $2.3 \times 10^{-12} \text{ m}^2/\text{s}$  at 1.04 wt.% H<sub>2</sub>O), using this mean value provides a reasonable approximation of the diffusivity over the whole profile. We note that taking the mean of the two end-member diffusivities additionally assumes that the nonlinearity of  $D_{\text{H}_2\text{O}_t}(c)$  is negligible. Using this method and fitting the diffusion model to the measured H<sub>2</sub>O depletion adjacent to the fracture/clast boundary of the CH5F and BTB tuffisites with the time as an adjustable parameter (and fitting using a least squares minimization method described above) yields times of ~4 and ~2 hr, respectively, for the time between fracture opening and final quenching (Figure 6c). It is important to highlight these timescales are *minima*, and they depend heavily on the model assumptions, such as the temperature. For example, Castro et al. (2012) showed that reducing the temperature by 200 °C increased this timescale from minutes to several tens of hours. Nevertheless, these predicted timescales compare well with other estimates of the lifetimes of tuffisites from Chaitén volcano (Castro et al., 2012).

### 5.4. The Lifespan of a Tuffisite

In the general conceptual scheme explored here, we envisage conduit-filling rhyolite lava that is periodically fractured by high-pressure gas and ash from below (e.g., Schipper et al., 2013). These processes involve the opening of the fracture, the transport of gas and ash, the clogging of the fracture, and a slower, time-dependent sintering of the fracture infill. In concert then, the outgassing time available for removing pressurized gas through the fractures is therefore the sum of the time from opening to clogging with pyroclastic debris,  $\lambda_1$ , and the time for sintering once the tuffisite is formed and welds shut,  $\lambda$ . The time  $\lambda_1$  from video footage of fractures opening and closing appears to be on the order of tens of seconds (Figure 1). The mass of gas and ash removed during this time, which could be used to compute the pressure decrease, is difficult to assess. But it is clear from the video footage (Figure 1; Schipper et al., 2013) that the outgassing continues, albeit more slowly, during the postclogging sintering of the fracture infill, with the emission of vapor only (i.e., without the ash phase).



Once the fracture has become clogged with pyroclastic debris, the process of sintering will act to reduce porosity and permeability toward zero. It is the timescale of sintering that is the key quantity in determining the efficacy of tuffisites as outgassing pathways after the open fracture is clogged with particles. In the absence of applied force on the sides of the fracture, the characteristic timescale associated with this process is the sintering timescale  $\lambda = R\mu/\Gamma$ , where  $\mu$  is the viscosity of the melt and  $\Gamma$  is the melt vapor surface tension.  $R$ , the mean grainsize, has been shown to capture sintering dynamics even in highly polydisperse distributions (Wadsworth, Vasseur, Llewellyn, & Dingwell, 2017). In other words, although estimates of  $R$  are small compared to the larger fragments readily identifiable in our microstructural work (Figures 3 and 4), it is the finer particle fraction that dictates the efficiency of viscous sintering—a result of the grainsize dependence of the sintering time (Gardner et al., 2018; Wadsworth et al., 2014; Wadsworth, Vasseur, Llewellyn, et al., 2016). When a force is applied to the fracture walls (such as a lithostatic pressure or the stress imparted by a recently opened adjacent fracture), however,  $\lambda$  will not be the controlling timescale, and the system is more likely to close over a compaction timescale  $\lambda_2 \approx \mu/(\sigma\alpha)$ , where  $\sigma$  is the applied stress (in Pa) on the fracture walls and  $\alpha$  is an empirical factor (Farquharson et al., 2017; Quane et al., 2009) that was calibrated for sintering polydisperse particles similar to the tuffisites studied here (the block-and-ash flow deposits from Mt. Meager; Figure 5) to be  $\alpha \approx 2$  (Heap et al., 2014). This is broadly similar to other compaction timescale approximations (Kennedy et al., 2016; McKenzie, 2011). If surface tension stress  $2\Gamma/R$  dominates over the stress applied to the fracture walls  $\sigma$ , then  $\lambda$  should be used. If instead the opposite is true, and the fracture wall stress dominates the surface tension stress, then  $\lambda_2$  should be used. In each respective case, the total outgassing time is  $\lambda_1 + \lambda$  or  $\lambda_1 + \lambda_2$ .

To illustrate how  $\lambda$  and  $\lambda_2$  vary, we take  $\Gamma = 0.3$  N/m for moderately dry rhyolites (Gardner & Ketcham, 2011). We note that  $\Gamma$  is significantly lower in rhyolites with up to ~4 wt.% dissolved water, but there are no measurements in the intermediate range of water contents, and these rhyolites are erupted close to the dry limit (Castro et al., 2014; Saubin et al., 2016). The melt viscosity of tuffisites from Chaitén (samples BTB and CH5F) and Cerdón Cauille (sample B1) can be estimated using a multicomponent viscosity model (Giordano et al., 2008), using major element composition (using the compositions provided in Castro & Dingwell, 2009, for Chaitén and in Alloway et al., 2015, for Cerdón Cauille), an inferred eruptive temperature of 825 °C for Chaitén (Castro & Dingwell, 2009) and 890 °C for Cerdón Cauille (Alloway et al., 2015; Castro et al., 2013), and measured H<sub>2</sub>O concentrations. H<sub>2</sub>O concentrations of 0.74 and 0.34 wt.% were taken for, respectively, the host obsidian and tuffisite in the BTB sample (Saubin et al., 2016, and 1.04 and 0.46 wt.% were taken for the host obsidian and tuffisite in the CH5F sample, see Figure 6c). For the B1 sample, measurements on eruptive products from the 2012–2013 Cerdón Cauille eruption provided a range of H<sub>2</sub>O concentration between 0.1 and 0.5 wt.% (Miltzer, 2013). The resulting viscosity range estimations were calculated to be  $10^{8.05} < \mu < 10^{9.07}$  Pa s for the BTB sample,  $10^{7.64} < \mu < 10^{8.65}$  Pa s for the CH5F sample, and  $10^{7.15} < \mu < 10^{8.23}$  Pa s for the B1 sample.

We assume, given the relationship between sintering timescale and grainsize (Wadsworth et al., 2014), that the viscosity of the fine-grained matrix controls viscous sintering. For the variability in  $R$  predicted here ( $2.5 < R < 15$   $\mu\text{m}$ ; Figure 5b), sintering times in the absence of applied forces  $\lambda$  are between 6 min and 5 hr, between 16 min and 13.6 hr, and between 2 min and 2.4 hr for CH5F, BTB, and B1 respectively (Figure 8). To compute  $\lambda_2$ , as a first-order estimate, we take  $\sigma = 2$  MPa, which is computed by matching the solubility of water (assuming 100% of the pressure is water vapor pressure) based on Liu et al. (2005), to the value measured at the tuffisite wall  $c_0$ . This yields values of  $\lambda_2$  (for the variability in  $R$  predicted here) between 11 s and 2 min, between 28 s and 5 min, and between 3.5 s and 42 s for CH5F, BTB, and B1 respectively (Figure 8). We again highlight that these timescales depend on the model input parameters: differences in viscosity (resulting from changes to the eruptive temperature and/or the water content, for example) can significantly modify these predictions. We also plot on Figure 8 an estimated range for the time from fracture opening to clogging with pyroclastic debris,  $\lambda_1$  (10–20 s, estimated using available video footage from Cerdón Cauille; Figure 1; Schipper et al., 2013) and the interfracture timescale ( $\lambda_1 + \lambda$  or  $\lambda_1 + \lambda_2$ ; 20–120 s; Schipper et al., 2013). These observed timescales are faster than the timescales solely predicted from surface tension and are much more consistent with the estimated range of compaction timescales (Figure 8), suggesting that compaction driven by the overburden (lithostatic) stress plays a key role in governing the lifetimes of these tuffisites. Although

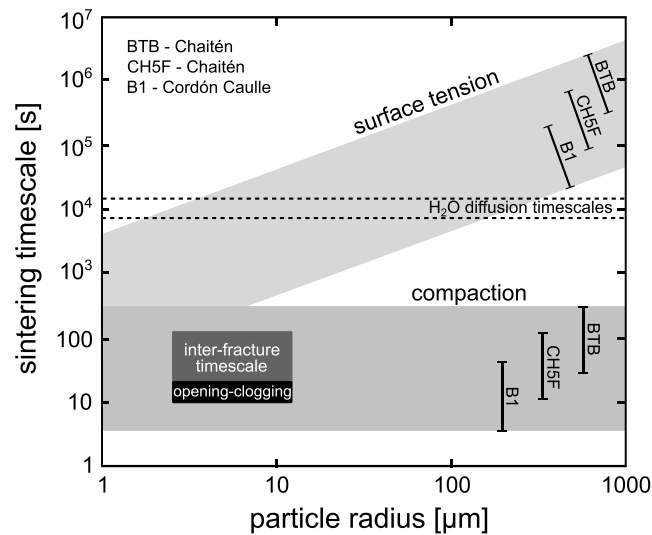


**Figure 8.** Sintering timescale as a function of particle radius for the two sintering regimes: surface tension and compaction (grey zones). Timescales are provided for tuffisites from Chaitén (samples BTB and CH5F) and Cordón Cauille (sample B1) using the range of viscosities determined using a multicomponent viscosity model (Giordano et al., 2008; see text for details). For the range of particle radii thought to control sintering in the tuffisites of this study ( $2.5 < R < 15 \mu\text{m}$ ; estimated using a permeability model for granular materials; Wadsworth, Vasseur, Scheu, et al., 2016; see Figure 5), the sintering times for the surface tension regime are between 6 min and 5 hr, between 16 min and 13.6 hr, and between 2 min and 2.4 hr for CH5F, BTB, and B1, respectively. Sintering times in the compaction regime are predicted to be between 11 s and 2 min, between 28 s and 5 min, and between 3.5 s and 42 s for CH5F, BTB, and B1, respectively. We also plot the estimated range for the time from fracture opening to clogging with pyroclastic debris,  $\lambda_1$  (10–20 s, estimated using video footage; Figure 1; Schipper et al., 2013) and the inter-fracture timescale ( $\lambda_1 + \lambda$  or  $\lambda_1 + \lambda_2$ ; 20–120 s; Schipper et al., 2013). The calculated diffusion timescales for BTB and CH5F (~2 and ~4 hr, respectively) are indicated by the dashed lines. As these relate to diffusive  $\text{H}_2\text{O}$  depletion in an approximately millimetric clast (BTB) and the tuffisite wall (CH5F), they are independent of the grainsize of the far finer-grained matrix (abscissa) and thus appear as horizontal lines.

depth estimations for tuffisites at Cordón Cauille are shallower (depth of about 50 m; Schipper et al., 2013) than those estimated for Chaitén, we note that a reduction in  $\sigma$  from 2 to 1 MPa only doubles the  $\lambda_2$  timescale and, even in this scenario, our estimated compaction timescales are still in line with the observed timescales. We further note that our estimated compaction timescales consider lithostatic pressures only and do not take stresses imparted by recently opened adjacent fractures into account.

$\text{H}_2\text{O}$  diffusion offers an independent tuffisite chronometer to these estimated viscous sintering timescales. The best fit diffusion model (Figure 6c) to the measured  $\text{H}_2\text{O}$  depletion adjacent to the fracture/clast boundary of the CH5F and BTB tuffisites yields timescales  $\lambda_d$  (time between fracture opening and final quenching) of ~4 and ~2 hr, respectively (as shown in the previous section). These predicted timescales compare well with other estimates of the lifetimes of tuffisites from Chaitén volcano and elsewhere (Berlo et al., 2013; Cabrera et al., 2011; Castro et al., 2012; Saubin et al., 2016). Further, we highlight that viscous sintering timescales were also found to coincide with  $\text{H}_2\text{O}$  re-equilibration timescales in obsidian pyroclasts from Mono Craters (United States) that were assembled from juvenile particles during magma ascent (Gardner et al., 2017), suggesting that viscous sintering plays an important role in cyclic fragmentation behavior and apparent open system degassing (Gardner et al., 2017; Rust et al., 2004; Tuffen et al., 2003; Watkins et al., 2017). Our predicted  $\text{H}_2\text{O}$  diffusion timescales are, however, longer than the observed interfracture timescales and the timescales predicted for compaction-driven sintering (Figure 8). Because  $\text{H}_2\text{O}$  diffusion can continue even after compaction renders permeable gas flow ineffective, we consider that  $\lambda_d$  is the sum of the fracture opening timescale ( $\lambda_1$ ), the sintering or compaction timescale ( $\lambda$  or  $\lambda_2$ ), and a quenching timescale. According to our analysis, the quenching timescale is therefore likely to be on the order of a couple of hours, consistent with conductive cooling of bombs tens of centimeters in diameter (e.g., Saubin et al., 2016). We also highlight the numerous model assumptions that may influence our predicted  $\text{H}_2\text{O}$  diffusion

timescales, such as, for example, using a steady eruptive temperature and a single step in H<sub>2</sub>O activity at the fracture walls. Furthermore, observations at Cordón Caulle highlight that ash jetting can occur from the same fracture and, since H<sub>2</sub>O diffusion would necessarily continue, the repeated use of the same fracture could also help explain the discrepancy between the H<sub>2</sub>O diffusion timescales and the timescales required for compaction, pressurization, and fragmentation.

### 5.5. Pressurization and Outgassing at Silicic Lava Flows and Domes

Before discussing the potential role of tuffisites in influencing conduit processes and outgassing during silicic eruptions, it is important to address the question: how common are tuffisites? Providing a robust answer to this question for active volcanoes such as Chaitén or Cordón Caulle is problematic, in part because fully mature, densely welded tuffisite is likely indistinguishable from dense obsidian (see Castro et al., 2014). Calculations presented in Castro et al. (2012) suggest that a dense spacing of tuffisites (approximately a tuffisite every 0.01–0.001 m) would be required to fully degas a silicic magma in the approximate times available. Such high tuffisite number densities are considered consistent with evidence that obsidian lavas have been thoroughly fractured and then rehealed (or annealed) to dense glass (Castro et al., 2012, 2014). Further, several field campaigns at Chaitén volcano have highlighted that bombs on the crater rim and flanks commonly host tuffisites, the width of which typically ranged from a couple of millimeters up to a few tens of millimeters. Evidence of high tuffisite number densities from dissected rhyolitic conduits in Iceland (McGowan, 2016) provides support to the high densities predicted for Chaitén volcano by Castro et al. (2012). For example, a 5-m line transect in a dissected rhyolitic conduit in Iceland contained 282 tuffisites (McGowan, 2016). Although the tuffisite number density from this dissected conduit may contain different generations of tuffisites (i.e., all 282 tuffisites may not have been active at the same time), this number speaks to the ubiquity, and therefore potential importance, of these features in rhyolitic conduits. We also note that even if tuffisites are relatively uncommon, their influence on the permeability of an otherwise impermeable magmatic plug can be very large. For example, a single permeable pathway within an large low-permeability rock mass can increase the equivalent permeability of the system by many orders of magnitude, as discussed in, for example, Heap and Kennedy (2016), Farquharson et al. (2017), and Farquharson and Wadsworth (2018). Finally, although the outgassing flux could be computed using either Darcy law (low Reynolds number) or the Forchheimer equation using the constraints of permeability provided herein, we note that while our determination of the porosity-permeability relationship is valid locally, the depth-dependent stress and the coupling between the evolving gas pressure and the sintering rates demands a full numerical solution (e.g., Michaut et al., 2013). We propose that fertile future research could use our model, validated using empirical data on tuffisites, to provide a tuffisite outgassing model for rhyolitic volcanoes.

In upper conduits characterized by dense, impermeable magmatic plugs and host rock (i.e., a “closed system”; see the modeling of Diller et al., 2006; Collinson & Neuberg, 2012), we propose here that the recurrence timescale of explosive venting must, in a broad sense, equal the sum of the timescales of tuffisite sintering, pressurization, and fragmentation. Our study provides estimates spanning seconds (in the case of compaction-driven sintering) to hours (in the case of surface tension-driven sintering) for the thorough sintering of tuffisites, and we can assume that the timescale for fragmentation is necessarily small compared to the other timescales. The timescale for pressurization, which will depend on, among other factors, the ascent rate and volatile budget of the magma, is the missing constraint. Therefore, the sintering times estimated herein must be less than or equal and cannot be longer than the explosive venting timescale. Indeed, the observed range of cyclic pressurization and ash venting timescales at erupting silicic lava domes at, for example, Santiaguillo volcano (Guatemala) and Soufrière Hills volcano (Montserrat; Holland et al., 2011; Johnson et al., 2008; Voight et al., 1999), is consistent with our timescale estimates for the thorough sintering of tuffisites. This may imply that pressurization timescales can be short or, and perhaps more likely, that pressurization begins before the tuffisites are completely sintered shut. Indeed, the presence of an H<sub>2</sub>O-rich clast population within the BTB sample demonstrated that deeper, pressurized gas entered the shallower, lower-pressure fracture system, consistent with the pressurization of fractures/tuffisites prior to the destruction of their permeability.

The low permeabilities attained by the CH5F ( $\sim 10^{-16}$  m<sup>2</sup>; Figure 5b and Table 1) and the BTB tuffisites ( $\sim 10^{-15}$  m<sup>2</sup>; Figure 5b and Table 1) coincide with that of healed gas escape routes modeled by Collinson



and Neuberg (2012). We consider that the effective healing of tuffisites likely therefore contributed to the upper conduit pressure accumulation that ultimately led to their explosive ejection. Although clast vesiculation contributed to porosity loss within the BTB tuffisite (alongside other mechanisms), the BTB tuffisite failed to attain the low permeability of CH5F, interpreted here as the result of a shorter pre-ejection healing time within the conduit. Nonetheless, the permeability attained by BTB ( $\sim 10^{-15} \text{ m}^2$ ) must have been sufficiently low to render gas loss inefficient over its lifespan (pressure equilibrium time at this permeability  $> 11$  days; see also the modeling of Collinson & Neuberg, 2012; Chevalier et al., 2017). We note that it is also possible that a healed tuffisite is not immediately ejected and undergoes additional viscous compaction prior to ejection in a later fragmentation event—a plausible scenario given the repetitive nature of tuffisite formation and healing (Tuffen et al., 2003). In this scenario, we would expect the diffusion timescale to greatly exceed the sintering timescale.

The modeled source depths of upper conduit pressurization are additionally consistent with ejected bomb depths at Chaitén volcano, as inferred from bomb volatile concentrations (see above and Saubin et al., 2016). It is therefore plausible that upper conduit pressurization cycles are modulated by sintering-driven blockage of initially permeable tuffisite networks, especially in crystal-poor rhyolitic systems where melt-rich magma readily sinters. Equivalent observational data from the 2008 eruption of Chaitén volcano is unfortunately lacking, but the filming of pulsatory ash venting during the eruption of Cordon Caulle in 2011–2012 revealed significantly shorter interexplosion intervals ( $< 40$  s, Schipper et al., 2013; Figure 1), perhaps controlled by the sintering of finer material. The rhyolite at Cordon Caulle is also of lower silica content than Chaitén volcano and was erupted at comparatively higher temperatures ( $\sim 890$  °C; Castro et al., 2013), factors that reduce melt viscosity and therefore sintering timescales (e.g., Gardner et al., 2018; Figure 8). Nonetheless, limited video footage prior to the onset of the hybrid phase at Chaitén volcano in 2008 (Figure 1b) records a key phase of eruption development, in which the initially broad pyroclastic vent had constricted to several distinct vents tens of meters across above the yet-to-emerge lava dome (also observed at Cordon Caulle). Such focusing of pyroclastic discharge requires sintering of initially loose pyroclastic vent-filling material to gain strength and reduce permeability (e.g., Heap et al., 2015; Kolzenburg et al., 2012; Kolzenburg & Russell, 2014). This indicates that sintering processes can act to reconfigure conduit architecture during eruptions, and the transition from initially Plinian to hybrid activity at Chaitén volcano can be conceptualized as a decrease in the width of venting tuffisites from the entire conduit, through an intermediate phase characterized by multiple vents tens of meters in breadth, to, finally, pathways only centimeters wide such as observed in the BTB tuffisite (Figure 2a). Occlusion of outgassing pathways by sintering encourages greater pressurization of the upper conduit, and this is proposed to be responsible for the forceful intrusion of a shallow laccolith at Cordon Caulle, whose emplacement coincided with a marked narrowing of the vent prior to the onset of hybrid activity (Castro et al., 2016).

The variable initial particle radius of a tuffisite relates to the efficiency of fragmentation (Kueppers et al., 2006), together with sorting phenomena associated with clastic transport and deposition (Tuffen et al., 2003). Fowler and Scheu (2016) demonstrate that for a given porosity, a larger overpressure release at fragmentation results in a smaller average grain size. Owing to the fact that viscous sintering timescales are shorter at small grain sizes (Gardner et al., 2018; Wadsworth et al., 2014; Wadsworth, Vasseur, Llewellyn, et al., 2016), we conclude that violent decompression events associated with fracture opening will create tuffisites capable of more rapid healing (for a given melt viscosity). As healing can provoke repressurization and explosive failure, the most energetic venting likely involves the shortest duration cycles of pyroclast and gas ejection from fracture systems.

The accuracy of the calculations presented herein invariably rests on the accuracy of the numerous model input parameters (such as the inferred temperatures used in our  $\text{H}_2\text{O}$  diffusion modeling and viscosity calculations) and, therefore, although we consider our assumptions as well reasoned, the model predictions should still be treated with some caution. Further outstanding complications include the time evolution of particle viscosity during sintering as diffusive mass transport of water occurs in tuffisites (Castro et al., 2014), grain size sorting during transport and accumulation of clastic particles (Tuffen & Dingwell, 2005), frictional heating and its potential role as a sintering accelerant, the entrainment of cooler lithics into tuffisites (although we highlight that lithics represent a very small fraction of the total fracture fill; e.g., Saubin et al., 2016, found that the lithic content of the BTB sample was  $< 0.5$  vol.%), and the effect of high particle-particle pressures in pore networks exceeding the capillary pressures of sintering (Wadsworth, Vasseur, Llewellyn, et al., 2016).

We further note that the tuffisites documented here are also end-members in that they are hosted in dense obsidian; tuffisites in other systems characterized by a more permeable host rock may behave and be preserved, differently (e.g., tuffisites in a pumiceous rhyolite host rock: Castro et al., 2012; the fractures documented at Volcán de Colima: Farquharson et al., 2016; Kendrick et al., 2016; Kolzenburg et al., 2012; or the fractures seen within pyroclasts from Katla, Iceland: Owen et al., 2019). Nevertheless, even in this scenario it is likely that the initially granular fracture fill will be of a higher permeability than the host rock. Therefore, although outgassing can occur through the host rock, we suggest that sintering timescales will be similar to those reported herein for rhyolitic systems and that tuffisites that form within a more permeable host rock will still play an important role in the cyclic bleeding and accumulation of pore pressure thought to drive episodic explosive events at active volcanoes. Indeed, connectivity between pumice-hosted tuffisites and exsolved gas in their vesicular walls can greatly facilitate outgassing and may be a key process assisting the formation of dense, compacted magma in shallow silicic conduits.

## 6. Concluding Remarks

We conclude that if fractures in silicic lavas, domes, and vents are primary outgassing pathways for local and deep-seated magma (Castro et al., 2014), then the longevity of open-system outgassing from those fractures will scale with the timescale of viscous sintering. Our analyses suggest that it is the timescale for sintering driven by compaction that provides the most realistic timescale estimates and is likely therefore an important process dictating the lifespan of these tuffisites. Importantly, the permeability of those fractures will decay toward zero over that same timescale, rendering outgassing ineffective and permitting the pore pressure to build, eventually driving subsequent explosions and rapid concomitant lava extrusion rates (e.g., Pallister et al., 2013). The grainsize dependence of viscous sintering (Gardner et al., 2018; Wadsworth et al., 2014; Wadsworth, Vasseur, Llewellyn, et al., 2016) suggests that the most energetic venting (i.e., the most efficient fragmentation; Kueppers et al., 2006) likely involves shorter duration cycles of pyroclast and gas ejection from fracture systems. The first-order constraint on lava and lava dome permeability evolution presented herein could be used to compare with cycles of proximal geophysical and geochemical signals such as conduit inflation, low-frequency seismicity, and surface emissions of gas and ash.

## Acknowledgments

M.J. Heap and H. Tuffen are indebted to the Royal Society International Exchanges program for funding our project entitled “Volcanic valves: The permeability of tuffisites.” H. Tuffen was additionally supported by a Royal Society University Research Fellowship and thanks Lancaster University Sports Centre and grounds staff for assistance. J.M. Castro thanks support from the VAMOS Research Center, University of Mainz. The first author acknowledges funding from an Initiative d'Excellence (IDEX) “Attractivité” grant VOLPERM (funded by the University of Strasbourg). We also thank Bertrand Renaudié, Jamie Farquharson, Jérémie Vasseur, Ed Llewellyn, Alexandra Kushnir, and Pauline Harlé. Gilles Morvan is thanked for technical support. The data collected for this study can be found in Table 1. The comments of two anonymous reviewers, the Associate Editor, and the Editor helped improve this manuscript.

## References

- Alloway, B. V., Pearce, N. J. G., Villarosa, G., Outes, V., & Moreno, P. I. (2015). Multiple melt bodies fed the AD 2011 eruption of Puyehue-Cordón Caulle, Chile. *Scientific Reports*, 5(1), 17589. <https://doi.org/10.1038/srep17589>
- ASTM D4404-10 (2010). *Standard test method for determination of pore volume and pore volume distribution of soil and rock by mercury intrusion porosimetry*. West Conshohocken, PA: ASTM International. [www.astm.org](http://www.astm.org)
- Behrens, H., & Nowak, M. (1997). The mechanisms of water diffusion in polymerized silicate melts. *Contributions to Mineralogy and Petrology*, 126(4), 377–385. <https://doi.org/10.1007/s004100050257>
- Berlo, K., Tuffen, H., Smith, V. C., Castro, J. M., Pyle, D. M., Mather, T. A., & Geraki, K. (2013). Element variations in rhyolitic magma resulting from gas transport. *Geochimica et Cosmochimica Acta*, 121, 436–451. <https://doi.org/10.1016/j.gca.2013.07.032>
- Black, B. A., Manga, M., & Andrews, B. (2016). Ash production and dispersal from sustained low-intensity Mono-Inyo eruptions. *Bulletin of Volcanology*, 78(8), 57. <https://doi.org/10.1007/s00445-016-1053-0>
- Cabrera, A., Weinberg, R. F., Wright, H. M., Zlotnik, S., & Cas, R. A. (2011). Melt fracturing and healing: A mechanism for degassing and origin of silicic obsidian. *Geology*, 39(1), 67–70. <https://doi.org/10.1130/G31355.1>
- Castro, J. M., Bindeman, I. N., Tuffen, H., & Schipper, C. I. (2014). Explosive origin of silicic lava: Textural and  $\delta D-H_2O$  evidence for pyroclastic degassing during rhyolite effusion. *Earth and Planetary Science Letters*, 405, 52–61. <https://doi.org/10.1016/j.epsl.2014.08.012>
- Castro, J. M., Cordonnier, B., Schipper, C. I., Tuffen, H., Baumann, T. S., & Feisel, Y. (2016). Rapid laccolith intrusion driven by explosive volcanic eruption. *Nature Communications*, 7, 13585. <https://doi.org/10.1038/ncomms13585>
- Castro, J. M., Cordonnier, B., Tuffen, H., Tobin, M. J., Puskar, L., Martin, M. C., & Bechtel, H. A. (2012). The role of melt-fracture degassing in defusing explosive rhyolite eruptions at volcán Chaitén. *Earth and Planetary Science Letters*, 333, 63–69. <https://doi.org/10.1016/j.epsl.2012.04.024>
- Castro, J. M., & Dingwell, D. B. (2009). Rapid ascent of rhyolitic magma at Chaitén volcano, Chile. *Nature*, 461(7265), 780. <https://doi.org/10.1038/nature08458>
- Castro, J. M., Schipper, C. I., Mueller, S. P., Militzer, A. S., Amigo, A., Parejas, C. S., & Jacob, D. (2013). Storage and eruption of near-liquidus rhyolite magma at Cordón Caulle, Chile. *Bulletin of Volcanology*, 75(4), 702.
- Chevalier, L., Collombet, M., & Pinel, V. (2017). Temporal evolution of magma flow and degassing conditions during dome growth, insights from 2D numerical modeling. *Journal of Volcanology and Geothermal Research*, 333, 116–133.
- Civan, F. (2010). Effective correlation of apparent gas permeability in tight porous media. *Transport in Porous Media*, 82(2), 375–384. <https://doi.org/10.1007/s11242-009-9432-z>
- Collinson, A. S. D., & Neuberg, J. W. (2012). Gas storage, transport and pressure changes in an evolving permeable volcanic edifice. *Journal of Volcanology and Geothermal Research*, 243, 1–13. <https://doi.org/10.1016/j.jvolgeores.2012.06.027>

- Crank, J. (1979). *The mathematics of diffusion*. Oxford, UK: Oxford University Press.
- Diller, K., Clarke, A. B., Voight, B., & Neri, A. (2006). Mechanisms of conduit plug formation: Implications for vulcanian explosions. *Geophysical Research Letters*, *33*, L20302. <https://doi.org/10.1029/2006GL027391>
- Eichelberger, J. C., Carrigan, C. R., Westrich, H. R., & Price, R. H. (1986). Non-explosive silicic volcanism. *Nature*, *323*(6089), 598. <https://doi.org/10.1038/323598a0>
- Farquharson, J. I., Heap, M. J., Lavallée, Y., Varley, N. R., & Baud, P. (2016). Evidence for the development of permeability anisotropy in lava domes and volcanic conduits. *Journal of Volcanology and Geothermal Research*, *323*, 163–185. <https://doi.org/10.1016/j.jvolgeores.2016.05.007>
- Farquharson, J. I., & Wadsworth, F. B. (2018). Upscaling permeability in anisotropic volcanic systems. *Journal of Volcanology and Geothermal Research*, *364*, 35–47. <https://doi.org/10.1016/j.jvolgeores.2018.09.002>
- Farquharson, J. I., Wadsworth, F. B., Heap, M. J., & Baud, P. (2017). Time-dependent permeability evolution in compacting volcanic fracture systems and implications for gas overpressure. *Journal of Volcanology and Geothermal Research*, *339*, 81–97. <https://doi.org/10.1016/j.jvolgeores.2017.04.025>
- Feng, S., Halperin, B. I., & Sen, P. N. (1987). Transport properties of continuum systems near the percolation threshold. *Physical Review B*, *35*(1), 197. <https://doi.org/10.1103/PhysRevB.35.197>
- Firouzi, M., Alnoaimi, K., Kovscek, A., & Wilcox, J. (2014). Klinkenberg effect on predicting and measuring helium permeability in gas shales. *International Journal of Coal Geology*, *123*, 62–68. <https://doi.org/10.1016/j.coal.2013.09.006>
- Forchheimer, P. (1901). Wasserbewegung durch boden. *Zeitschrift des Vereins Deutscher Ingenieure*, *45*, 1782–1788.
- Fowler, A. C., & Scheu, B. (2016). A theoretical explanation of grain size distributions in explosive rock fragmentation. *Proceedings of the Royal Society A*, *472*(2190), 20150843. <https://doi.org/10.1098/rspa.2015.0843>
- Gardner, J. E., & Ketcham, R. A. (2011). Bubble nucleation in rhyolite and dacite melts: Temperature dependence of surface tension. *Contributions to Mineralogy and Petrology*, *162*(5), 929–943. <https://doi.org/10.1007/s00410-011-0632-5>
- Gardner, J. E., Llewellyn, E. W., Watkins, J. M., & Befus, K. S. (2017). Formation of obsidian pyroclasts by sintering of ash particles in the volcanic conduit. *Earth and Planetary Science Letters*, *459*, 252–263. <https://doi.org/10.1016/j.epsl.2016.11.037>
- Gardner, J. E., Wadsworth, F. B., Llewellyn, E. W., Watkins, J. M., & Coumans, J. P. (2018). Experimental sintering of ash at conduit conditions and implications for the longevity of tuffisites. *Bulletin of Volcanology*, *80*(3), 23. <https://doi.org/10.1007/s00445-018-1202-8>
- Giordano, D., Russell, J. K., & Dingwell, D. B. (2008). Viscosity of magmatic liquids: A model. *Earth and Planetary Science Letters*, *271*(1–4), 123–134. <https://doi.org/10.1016/j.epsl.2008.03.038>
- Gonnermann, H. M., & Manga, M. (2003). Explosive volcanism may not be an inevitable consequence of magma fragmentation. *Nature*, *426*(6965), 432. <https://doi.org/10.1038/nature02138>
- Heap, M., Reuschlé, T., Baud, P., Renard, F., & Iezzi, G. (2018). The permeability of stylolite-bearing limestone. *Journal of Structural Geology*, *116*, 81–93. <https://doi.org/10.1016/j.jsg.2018.08.007>
- Heap, M. J. (2019). The influence of sample geometry on the permeability of a porous sandstone. *Geoscientific Instrumentation, Methods and Data Systems*, *8*(1), 55–61. <https://doi.org/10.5194/gi-8-55-2019>
- Heap, M. J., Farquharson, J. I., Wadsworth, F. B., Kolzenburg, S., & Russell, J. K. (2015). Timescales for permeability reduction and strength recovery in densifying magma. *Earth and Planetary Science Letters*, *429*, 223–233. <https://doi.org/10.1016/j.epsl.2015.07.053>
- Heap, M. J., & Kennedy, B. M. (2016). Exploring the scale-dependent permeability of fractured andesite. *Earth and Planetary Science Letters*, *447*, 139–150. <https://doi.org/10.1016/j.epsl.2016.05.004>
- Heap, M. J., Kolzenburg, S., Russell, J. K., Campbell, M. E., Welles, J., Farquharson, J. I., & Ryan, A. (2014). Conditions and timescales for welding block-and-ash flow deposits. *Journal of Volcanology and Geothermal Research*, *289*, 202–209. <https://doi.org/10.1016/j.jvolgeores.2014.11.010>
- Heap, M. J., Kushnir, A. R., Gilg, H. A., Wadsworth, F. B., Reuschlé, T., & Baud, P. (2017). Microstructural and petrophysical properties of the Permo-Triassic sandstones (Buntsandstein) from the Soultz-sous-Forêts geothermal site (France). *Geothermal Energy*, *5*(1), 26. <https://doi.org/10.1186/s40517-017-0085-9>
- Heap, M. J., Reuschlé, T., Farquharson, J. I., & Baud, P. (2018). Permeability of volcanic rocks to gas and water. *Journal of Volcanology and Geothermal Research*, *354*, 29–38. <https://doi.org/10.1016/j.jvolgeores.2018.02.002>
- Heiken, G., Wohletz, K., & Eichelberger, J. (1988). Fracture fillings and intrusive pyroclasts, Inyo Domes, California. *Journal of Geophysical Research*, *93*(B5), 4335–4350. <https://doi.org/10.1029/JB093iB05p04335>
- Heller, R., Vermilyen, J., & Zoback, M. (2014). Experimental investigation of matrix permeability of gas shales. *AAPG Bulletin*, *98*(5), 975–995. <https://doi.org/10.1306/09231313023>
- Holland, A. P., Watson, I. M., Phillips, J. C., Caricchi, L., & Dalton, M. P. (2011). Degassing processes during lava dome growth: Insights from Santiaguito lava dome, Guatemala. *Journal of Volcanology and Geothermal Research*, *202*(1–2), 153–166. <https://doi.org/10.1016/j.jvolgeores.2011.02.004>
- Ihinger, P. D., Hervig, R. L., & McMillan, P. F. (1994). Analytical methods for volatiles in glasses. *Reviews in Mineralogy and Geochemistry*, *30*(1), 67–121.
- Johnson, J. B., Lees, J. M., Gerst, A., Sahagian, D., & Varley, N. (2008). Long-period earthquakes and co-eruptive dome inflation seen with particle image velocimetry. *Nature*, *456*(7220), 377. <https://doi.org/10.1038/nature07429>
- Kemmer, G., & Keller, S. (2010). Nonlinear least-squares data fitting in Excel spreadsheets. *Nature Protocols*, *5*(2), 267. <https://doi.org/10.1038/nprot.2009.182>
- Kendrick, J. E., Lavallée, Y., Varley, N. R., Wadsworth, F. B., Lamb, O. D., & Vasseur, J. (2016). Blowing off steam: Tuffsite formation as a regulator for lava dome eruptions. *Frontiers in Earth Science*, *4*, 41. <https://doi.org/10.3389/feart.2016.00041>
- Kennedy, B. M., Wadsworth, F. B., Vasseur, J., Schipper, C. I., Jellinek, A. M., von Aulock, F. W., et al. (2016). Surface tension driven processes densify and retain permeability in magma and lava. *Earth and Planetary Science Letters*, *433*, 116–124. <https://doi.org/10.1016/j.epsl.2015.10.031>
- Klinkenberg, L. J. (1941). The permeability of porous media to liquids and gases. In *Drilling and production practice*. (pp. 200–213). New York: American Petroleum Institute.
- Kolzenburg, S., Heap, M., Lavallée, Y., Russell, J., Meredith, P., & Dingwell, D. B. (2012). Strength and permeability recovery of tuffsite-bearing andesite. *Solid Earth*, *3*, 191–198. <https://doi.org/10.5194/se-3-191-2012>
- Kolzenburg, S., & Russell, J. K. (2014). Welding of pyroclastic conduit infill: A mechanism for cyclical explosive eruptions. *Journal of Geophysical Research: Solid Earth*, *119*, 5305–5323. <https://doi.org/10.1002/2013JB010931>



- Kueppers, U., Scheu, B., Spieler, O., & Dingwell, D. B. (2006). Fragmentation efficiency of explosive volcanic eruptions: a study of experimentally generated pyroclasts. *Journal of Volcanology and Geothermal Research*, *153*(1-2), 125–135. <https://doi.org/10.1016/j.jvolgeores.2005.08.006>
- Kushnir, A. R., Martel, C., Champallier, R., & Arbaret, L. (2017). In situ confirmation of permeability development in shearing bubble-bearing melts and implications for volcanic outgassing. *Earth and Planetary Science Letters*, *458*, 315–326. <https://doi.org/10.1016/j.epsl.2016.10.053>
- Lara, L. E. (2009). The 2008 eruption of the Chaitén Volcano, Chile: A preliminary report. *Andean Geology*, *36*(1), 125–130. <https://doi.org/10.5027/andgeoV36n1-a09>
- Latham, E. A., & Bustin, R. M. (2016). Klinkenberg gas slippage measurements as a means for shale pore structure characterization. *Geofluids*, *16*(2), 264–278. <https://doi.org/10.1111/gfl.12147>
- Liu, Y., Zhang, Y., & Behrens, H. (2005). Solubility of H<sub>2</sub>O in rhyolitic melts at low pressures and a new empirical model for mixed H<sub>2</sub>O–CO<sub>2</sub> solubility in rhyolitic melts. *Journal of Volcanology and Geothermal Research*, *143*(1), 219–235.
- McGowan, E. (2016). Magma emplacement and deformation in rhyolitic dykes: Insight into magmatic outgassing. (PhD thesis). UK: Lancaster University.
- McKenzie, D. (2011). Compaction and crystallization in magma chambers: Towards a model of the Skaergaard intrusion. *Journal of Petrology*, *52*(5), 905–930. <https://doi.org/10.1093/petrology/egr009>
- Michaut, C., Ricard, Y., Bercovici, D., & Sparks, R. S. J. (2013). Eruption cyclicity at silicic volcanoes potentially caused by magmatic gas waves. *Nature Geoscience*, *6*(10), 856.
- Militzer, A. S. (2013). The P-T-x evolution of the 2011–12 explosively and effusively erupted rhyolites at Puyehue-Cordón Caulle, Chile. Diplomarbeit, Univ. Mainz, 93 pp.
- Nara, Y., Meredith, P. G., Yoneda, T., & Kaneko, K. (2011). Influence of macro-fractures and micro-fractures on permeability and elastic wave velocities in basalt at elevated pressure. *Tectonophysics*, *503*(1-2), 52–59. <https://doi.org/10.1016/j.tecto.2010.09.027>
- Newman, S., Stolper, E. M., & Epstein, S. (1986). Measurement of water in rhyolitic glasses; calibration of an infrared spectroscopic technique. *American Mineralogist*, *71*(11-12), 1527–1541.
- Okumura, S., Nakamura, M., & Nakashima, S. (2003). Determination of molar absorptivity of IR fundamental OH-stretching vibration in rhyolitic glasses. *American Mineralogist*, *88*(11-12), 1657–1662. <https://doi.org/10.2138/am-2003-11-1204>
- Okumura, S., & Sasaki, O. (2014). Permeability reduction of fractured rhyolite in volcanic conduits and its control on eruption cyclicity. *Geology*, *42*(10), 843–846. <https://doi.org/10.1130/G35855.1>
- Owen, J., Shea, T., & Tuffen, H. (2019). Basalt, unveiling fluid-filled fractures, inducing sediment intra-void transport, ephemerally: Examples from Katla 1918. *Journal of Volcanology and Geothermal Research*, *369*, 121–144. <https://doi.org/10.1016/j.jvolgeores.2018.11.002>
- Pallister, J. S., Diefenbach, A. K., Burton, W. C., Muñoz, J., Griswold, J. P., Lara, L. E., et al. (2013). The Chaitén rhyolite lava dome: Eruption sequence, lava dome volumes, rapid effusion rates and source of the rhyolite magma. *Andean Geology*, *40*(2), 277–294. <https://doi.org/10.5027/andgeoV40n2-a06>
- Quane, S. L., Russell, J. K., & Friedlander, E. A. (2009). Time scales of compaction in volcanic systems. *Geology*, *37*(5), 471–474. <https://doi.org/10.1130/G25625A.1>
- Rintoul, M. D. (2000). Precise determination of the void percolation threshold for two distributions of overlapping spheres. *Physical Review E*, *62*(1), 68. <https://doi.org/10.1103/PhysRevE.62.68>
- Russell, J. K., & Quane, S. L. (2005). Rheology of welding: Inversion of field constraints. *Journal of Volcanology and Geothermal Research*, *142*(1-2), 173–191. <https://doi.org/10.1016/j.jvolgeores.2004.10.017>
- Rust, A. C., Cashman, K. V., & Wallace, P. J. (2004). Magma degassing buffered by vapor flow through brecciated conduit margins. *Geology*, *32*(4), 349. <https://doi.org/10.1130/G20388.2>
- Ryan, A. G., Friedlander, E. A., Russell, J. K., Heap, M. J., & Kennedy, L. A. (2018). Hot pressing in conduit faults during lava dome extrusion: Insights from Mount St. Helens 2004–2008. *Earth and Planetary Science Letters*, *482*, 171–180. <https://doi.org/10.1016/j.epsl.2017.11.010>
- Ryan, A. G., Russell, J. K., & Heap, M. J. (2018). Rapid solid-state sintering in volcanic systems. *American Mineralogist*, *103*(12), 2028–2031. <https://doi.org/10.2138/am-2018-6714>
- Ryan, A. G., Russell, J. K., Heap, M. J., Kolzenburg, S., Vona, A., & Kushnir, A. R. L. (2019). Strain-dependent rheology of silicate melt foams: importance for outgassing of silicic lavas. *Journal of Geophysical Research: Solid Earth*, *124*. <https://doi.org/10.1029/2019JB018099>
- Saubin, E., Tuffen, H., Gurioli, L., Owen, J., Castro, J. M., Berlo, K., et al. (2016). Conduit dynamics in transitional rhyolitic activity recorded by tuffsite vein textures from the 2008–2009 Chaitén Eruption. *Frontiers in Earth Science*, *4*, 59. <https://doi.org/10.3389/feart.2016.00059>
- Schipper, C. I., Castro, J. M., Tuffen, H., James, M. R., & How, P. (2013). Shallow vent architecture during hybrid explosive–effusive activity at Cordón Caulle (Chile, 2011–12): Evidence from direct observations and pyroclast textures. *Journal of Volcanology and Geothermal Research*, *262*, 25–37. <https://doi.org/10.1016/j.jvolgeores.2013.06.005>
- Stasiuk, M. V., Barclay, J., Carroll, M. R., Jaupart, C., Ratté, J. C., Sparks, R. S. J., & Tait, S. R. (1996). Degassing during magma ascent in the Mule Creek vent (USA). *Bulletin of Volcanology*, *58*(2-3), 117–130. <https://doi.org/10.1007/s004450050130>
- Stix, J., Zapata, G. J. A., Calvache, V. M., Cortés, J. G. P., Fischer, T. P., Gómez, M. D., et al. (1993). A model of degassing at Galeras Volcano, Colombia, 1988–1993. *Geology*, *21*(11), 963–967. [https://doi.org/10.1130/0091-7613\(1993\)021<0963:AMODAG>2.3.CO;2](https://doi.org/10.1130/0091-7613(1993)021<0963:AMODAG>2.3.CO;2)
- Torquato, S. (2013). *Random heterogeneous materials: Microstructure and macroscopic properties*, (Vol. 16). New York: Springer Science & Business Media.
- Torquato, S., & Avellaneda, M. (1991). Diffusion and reaction in heterogeneous media: Pore size distribution, relaxation times, and mean survival time. *The Journal of Chemical Physics*, *95*(9), 6477–6489. <https://doi.org/10.1063/1.461519>
- Tuffen, H., & Dingwell, D. (2005). Fault textures in volcanic conduits: evidence for seismic trigger mechanisms during silicic eruptions. *Bulletin of Volcanology*, *67*(4), 370–387. <https://doi.org/10.1007/s00445-004-0383-5>
- Tuffen, H., Dingwell, D. B., & Pinkerton, H. (2003). Repeated fracture and healing of silicic magma generate flow banding and earthquakes? *Geology*, *31*(12), 1089–1092. DOI. <https://doi.org/10.1130/G19777.1>
- Vasseur, J., Wadsworth, F. B., Lavallée, Y., Hess, K. U., & Dingwell, D. B. (2013). Volcanic sintering: timescales of viscous densification and strength recovery. *Geophysical Research Letters*, *40*, 5658–5664. <https://doi.org/10.1002/2013GL058105>
- Voight, B., Sparks, R. S. J., Miller, A. D., Stewart, R. C., Hoblitt, R. P., Clarke, A., et al. (1999). Magma flow instability and cyclic activity at Soufriere Hills volcano, Montserrat, British West Indies. *Science*, *283*(5405), 1138–1142. <https://doi.org/10.1126/science.283.5405.1138>

- von Aulock, F. W., Kennedy, B. M., Schipper, C. I., Castro, J. M., Martin, D. E., Oze, C., et al. (2014). Advances in Fourier transform infrared spectroscopy of natural glasses: From sample preparation to data analysis. *Lithos*, 206-207, 52-64. <https://doi.org/10.1016/j.lithos.2014.07.017>
- Wadsworth, F. B., Vasseur, J., Llewellyn, E. W., & Dingwell, D. B. (2017). Sintering of polydisperse viscous droplets. *Physical Review E*, 95(3), 033114. <https://doi.org/10.1103/PhysRevE.95.033114>
- Wadsworth, F. B., Vasseur, J., Llewellyn, E. W., Schaubroth, J., Dobson, K. J., Scheu, B., & Dingwell, D. B. (2016). Sintering of viscous droplets under surface tension. *Proceedings of the Royal Society A*, 472(2188), 20150780. <https://doi.org/10.1098/rspa.2015.0780>
- Wadsworth, F. B., Vasseur, J., Scheu, B., Kendrick, J. E., Lavallée, Y., & Dingwell, D. B. (2016). Universal scaling of fluid permeability during volcanic welding and sediment diagenesis. *Geology*, 44(3), 219-222. <https://doi.org/10.1130/G37559.1>
- Wadsworth, F. B., Vasseur, J., von Aulock, F. W., Hess, K. U., Scheu, B., Lavallée, Y., & Dingwell, D. B. (2014). Nonisothermal viscous sintering of volcanic ash. *Journal of Geophysical Research: Solid Earth*, 119, 8792-8804. <https://doi.org/10.1002/2014JB011453>
- Watkins, J. M., Gardner, J. E., & Befus, K. S. (2017). Nonequilibrium degassing, regassing, and vapor fluxing in magmatic feeder systems. *Geology*, 45(2), 183-186. <https://doi.org/10.1130/G38501.1>
- Zhang, Y. (1999). H<sub>2</sub>O in rhyolitic glasses and melts: measurement, speciation, solubility, and diffusion. *Reviews of Geophysics*, 37(4), 493-516. <https://doi.org/10.1029/1999RG900012>